JGR Space Physics

RESEARCH ARTICLE
10.1029/2020JA028474

Key Points:

- A magnetic cloud produces an ion foreshock populated with ultralow frequency (ULF) waves with higher frequencies and wider spectral widths than usual
- In the magnetosphere and on the ground, ULF waves are detected in a wide frequency range of ~5 mHz–120 mHz
- Numerical simulation indicates short spatial scales, as well as multiple frequencies, of the foreshock waves

Correspondence to:
K. Takahashi,
kazue.takahashi@jhuapl.edu

Citation:
Takahashi, K., Turc, L., Kilpua, E., Takahashi, N., Dimmock, A., Kajdic, P., et al. (2021). Propagation of ultralow-frequency waves from the ion foreshock into the magnetosphere during the passage of a magnetic cloud. *Journal of Geophysical Research: Space Physics*, *126*, e2020JA028474. https://doi.org/10.1029/2020JA028474

Received 13 JUL 2020
Accepted 13 DEC 2020

Propagation of Ultralow-Frequency Waves from the Ion Foreshock into the Magnetosphere During the Passage of a Magnetic Cloud

Kazue Takahashi[1], Lucile Turc[2], Emilia Kilpua[2], Naoko Takahashi[3], Andrew Dimmock[4], Primoz Kajdic[5], Minna Palmroth[2,6], Yann Pfau-Kempf[2], Jan Soucek[7], Tetsuo Motoba[1], Michael D. Hartinger[8,9], Anton Artemyev[10], Howard Singer[11], Urs Ganse[2], and Markus Battarbee[2]

[1]The Johns Hopkins University Applied Physics Laboratory, Laurel, MD, USA, [2]Department of Physics, University of Helsinki, Helsinki, Finland, [3]Department of Earth and Planetary Science, Graduate School of Science, the University of Tokyo, Tokyo, Japan, [4]Swedish Institute of Space Physics (IRF), Uppsala, Sweden, [5]Instituto de Geofísica, Universidad Nacional Autónoma de México, Ciudad Universitaria, Ciudad de México, Mexico, [6]Finnish Meteorological Institute, Helsinki, Finland, [7]Institute of Atmospheric Physics, Academy of Sciences of the Czech Republic, Prague, Czech Republic, [8]Space Science Institute, Boulder, CO, USA, [9]Virginia Polytechnic Institute and State University, Blacksburg, VA, USA, [10]University of California, Los Angeles, CA, USA, [11]Space Weather Prediction Center, National Oceanic and Atmospheric Administration (NOAA), Boulder, CO, USA

Abstract We have examined the properties of ultralow-frequency (ULF) waves in space (the ion foreshock, magnetosheath, and magnetosphere) and at dayside magnetometer stations (L = 1.6–6.5) during Earth's encounter with a magnetic cloud in the solar wind, which is characterized by magnetic fields with large magnitudes (~14 nT) and small cone angles (~30°). In the foreshock, waves were excited at ~90 m Hz as expected from theory, but there were oscillations at other frequencies as well. Oscillations near 90 mHz were detected at the other locations in space, but they were not in general the most dominant oscillations. On the ground, pulsations in the approximate Pc2–Pc4 band (5 mHz–120 mHz) were continuously detected at all stations, with no outstanding spectral peaks near 90 mHz in the H component except at stations where the frequency of the third harmonic of standing Alfvén waves had this frequency. The fundamental toroidal wave frequency was below 90 mHz at all stations. In the D component spectra, a minor spectral peak is found near 90 mHz at stations located at $L < 3$, and the power dropped abruptly above this frequency. Magnetospheric compressional wave power was much weaker on the nightside. A hybrid-Vlasov simulation indicates that foreshock ULF waves have short spatial scale lengths and waves transmitted into the magnetosphere are strongly attenuated away from noon.

1. Introduction

Ultralow frequency (ULF) waves are permanently present in the ion foreshock region (Fairfield, 1969). The waves, which we call "foreshock waves" in this study instead of a commonly used alternative "upstream waves," are excited through an instability caused by ions streaming from the bow shock back into the solar wind (Barnes, 1970; Fairfield, 1969; Hoppe et al., 1981; Kovner et al., 1976). Because the location of the foreshock boundary depends on the orientation of the interplanetary magnetic field (IMF), the spatial extent of the region populated by the foreshock waves depends on the IMF as well. When the IMF is nearly parallel to the Earth-Sun line, the foreshock occupies a large volume in front of the bow shock nose. When the IMF is nearly perpendicular to the Sun-Earth line, the foreshock near noon is very limited in volume, meaning reduced impact of the waves on the magnetosphere. Troitskaya et al. (1971) noted that ground magnetic pulsations in the Pc4 (7 mHz–22 mHz), Pc3 (22 mHz–100 mHz), and Pc2 (100 mHz–200 mHz) bands are suppressed when the IMF is in the latter configuration and suggested that the foreshock waves are the source of the pulsations. This IMF orientation effect has been confirmed in many subsequent studies (e.g., Greenstadt & Olson, 1976; Russell et al., 1983; Wolfe et al., 1980).

The foreshock source mechanism for Pc2–Pc4 pulsations also means that the pulsation frequency depends on the magnitude or total intensity (denoted B_t; the suffix "t" is not to be taken for "tangential") of the IMF. Statistical studies (e.g., Troitskaya et al., 1971) found that the pulsation frequency can be expressed in the

form $f(\mathrm{mHz}) = cB_t(\mathrm{nT})$, where c is a constant in the range 5–8. The empirical formula can be explained by theoretical consideration of wave generation through an ion cyclotron instability. For example, Takahashi et al. (1984) derived a theoretical foreshock wave frequency f_{fw} given by

$$f_{fw}(\mathrm{mHz}) = 7.6B_t(\mathrm{nT})\cos^2\theta_{xB}, \quad (1)$$

where θ_{xB} is the angle between the IMF and the Earth-Sun line, called the IMF cone angle.

In our current understanding, foreshock waves propagate sunward in the plasma rest frame are advected antisunward by the super Alfvénic solar wind, enter the magnetosheath, and impact the magnetosphere. Within the magnetosphere, the transmitted waves propagate across the background magnetic field in the magnetohydrodynamic (MHD) fast mode (Heilig et al., 2007; Yumoto et al., 1984, 1985). The fast mode waves also couple to Alfvén waves (Takahashi et al., 1984). Both wave modes reach the ground and produce magnetic pulsations (Yumoto & Saito, 1983). Commonly cited evidence of propagation of foreshock waves into the magnetosphere is the detection of foreshock waves and ground pulsations at the same frequency (Clausen et al., 2009; Engebretson et al., 1987; Verõ et al., 1998).

While the above scenario for wave excitation and propagation is widely accepted, more quantitative understanding of the three-dimensional (3-D) propagation of foreshock ULF waves into the magnetosphere is challenging. One reason is that the wave generation is a kinetic process whereas the magnetospheric propagation is an MHD process. Also, the 3-D geometry of the foreshock, magnetosheath, and magnetosphere compounds the problem because a ray-tracing approach is not applicable to magnetospheric Pc2–Pc4 waves, which have wavelengths comparable to the scale size of the magnetosphere.

The present study is motivated by recent studies showing that foreshock wave activity can be significantly modified during intervals of enhanced IMF magnitude, as encountered at Earth during magnetic cloud events (Turc et al., 2018, 2019). Magnetic clouds are a subset of interplanetary coronal mass ejections (ICMEs) in which a clear flux rope structure is observed (Burlaga et al., 1981). They result in a sustained enhancement of the IMF magnitude, above 10 nT, lasting from several hours to several days. Numerical simulations and spacecraft observations revealed that not only do magnetic clouds increase the wave frequency, as expected from earlier works (Takahashi et al., 1984), but they also lead to more complex wave activity. Instead of the typical quasi monochromatic waves (Eastwood et al., 2005), the foreshock is populated with a superposition of waves at different frequencies during magnetic clouds (Turc et al., 2019).

We analyzed ULF waves associated with this unusual foreshock wave activity during magnetic clouds with the goal of understanding how the waves propagate from the source region in the ion foreshock into various regions in the magnetosphere. We selected the time interval 1000 UT–1200 UT on July 20, 2016, during which a magnetic cloud was interacting with near-Earth space. In this interval, two spacecraft were either in the foreshock or in the magnetosheath, one spacecraft was in the dayside magnetosphere, and three spacecraft were in the night-side magnetosphere. In addition, a ground magnetometer array covering a wide range of latitudes provided ground pulsation data on the dayside. These observations allow us to obtain detailed information on the global propagation of waves generated in the foreshock and to compare the results with a numerical simulation performed with the hybrid-Vlasov model Vlasiator (Palmroth et al., 2018; von Alfthan et al., 2014). The target of our simulation is the properties of magnetospheric ULF waves that are excited when the magnetosphere is under the influence of a magnetic cloud. We are now interested in finding out whether magnetospheric ULF waves also exhibit complex spectra during the passage of a magnetic cloud.

The remainder of the study is organized as follows. Section 2 describes the experiments and data. Section 3 presents background information for the wave event selected for study. Sections 4–6 describe the waves. Section 7 presents the simulation results. Section 8 presents discussion, and Section 9 presents conclusions.

2. Experiments and Data

Spacecraft data used in the study include electric field (E), magnetic field (B), and ion plasma bulk parameters from three Time History of Events and Macroscale Interactions during Substorms (THEMIS) spacecraft (Auster et al., 2008; Bonnell et al., 2008; McFadden et al., 2008) and three Geostationary Operational Envi-

ronmental Satellite (GOES) spacecraft (Singer et al., 1996). In addition, we use the solar wind OMNI data, which are generated by combining data from multiple spacecrafts (King & Papitashvili, 2005). The source of ground magnetic field data is the European quasi Meridian magnetometer array (EMMA; Lichtenberger et al., 2013). The ground magnetic field is given using the locally defined magnetic northward (H) and eastward (D) components in the horizontal plane.

We examine ULF waves at frequencies mainly below 150 mHz, which requires the data sampling period to be 3.33 s or shorter. To this end, we use field data from THEMIS-A and THEMIS-D provided with the time resolution of the spacecraft spin period (~3 s). For THEMIS-E, which had a spin period of 4.14 s, we start from high-time resolution (0.062 s) samples, take running averages of the data to suppress aliasing, and downsample the data to the time resolution appropriate for spectral analysis. Other data are 0.5 s samples from GOES and 1 s samples from the ground magnetometers.

We obtain power spectra using the standard Fourier transform method. To eliminate the effect of slow temporal or spatial variations, we subtract a trend function from each field component. The function is a polynomial of the form $c_0 + c_1\tau + c_2\tau^2$ fitted to the observational data, where τ is UT (t) rescaled to the range from −0.5 to 0.5 for the time interval (t_0–t_1) selected, that is, $\tau = -0.5 + (t - t_0)/(t_1 - t_0)$. The coefficients c_0, c_1, and c_2 are determined using the least squares method.

3. Observation Background

3.1. Solar Wind and Geomagnetic Conditions

Figure 1 shows an overview of the solar wind conditions and geomagnetic activity for a 24 h interval including the 2 h interval (1000 UT–1200 UT on July 20, shaded green) selected for the detailed analysis. An interplanetary shock wave driven by an ICME is detected at 2355 UT on July 19. The shock is followed by a sheath featuring a very high proton density (n_p exceeding 50 cm^{-3}) and high magnetic field variability. The ICME ejecta starts at ~8 UT on July 20 (see e.g., the online catalog by Richardson and Cane [http://www.srl.caltech.edu/ACE/ASC/DATA/level3/icmetable2.htm]) and is characterized by lower field variability, some smooth rotation of the field direction, and lower density. These are signatures for magnetic clouds (Burlaga et al., 1981). We note that the structure of the ICME ejecta is complex, but we do not analyze it here further. Rather, we focus on the ending part of the ICME ejecta, that is, the green-shaded region. At 1000 UT–1200 UT, B_t is ~14 nT, which is above the average solar wind value, a large B_x component, a very small B_z component, and a low variability (δB). The dominance of B_x means low θ_{xB} (Figure 1h) and a large ion foreshock region upstream of the bow shock nose. The large B_t means high ULF wave frequencies in the foreshock (see the Introduction) if the frequencies are related to the ion cyclotron frequency. According to Equation 1, we can expect to see wave power at higher frequencies than normal, up to ~100 mHz (period of 10 s). After 1200 UT, the field is turbulent and θ_{xB} increases.

Although the magnetic field in the sheath and in the front part of the ICME was high (reaching nearly 30 nT), only weak geomagnetic activity followed as the field was directed predominantly northward. However, several weak/moderate-level substorms occurred with peak AL approximately −500 nT. SYM-H (Figure 1k) reached −25 nT, that is, it stayed above the weak storm limit (−30 nT). However, by the beginning of the selected 2 h interval, geomagnetic activity became very quiet. During 1000 UT–1200 UT (green-shaded region), SYM-H stayed between −16 nT and −5 nT, AL stayed between −42 nT and −4 nT, and the H component at the Masi station (MAS, $L = 6.4$, noon sector) changed little (39 nT). Figure 1i shows that the bow shock stand-off distance is ~11 R_E according to Equation 4 of Farris and Russell (1994), where R_E is the Earth's radius. Figure 1j shows that the magnetopause distance is ~8 R_E according to Equation 10 of Shue et al. (1998). During the sheath and ICME, both distances are substantially lower than under average solar wind conditions (14.6 R_E and 11.0 RE, respectively, according to Fairfield [1971]) because of the large dynamic pressure (varying between ~7 nPa and ~25 nPa, not shown).

In summary, the solar wind and geomagnetic activity context for the analyzed period consists of a quiet magnetosphere during magnetic cloud-like solar wind driving conditions, that is, featuring enhanced and smooth magnetic fields and low variance of solar wind plasma parameters. In the remainder of this study, we focus on spacecraft and ground observations made at 1000 UT–1200 UT on July 20.

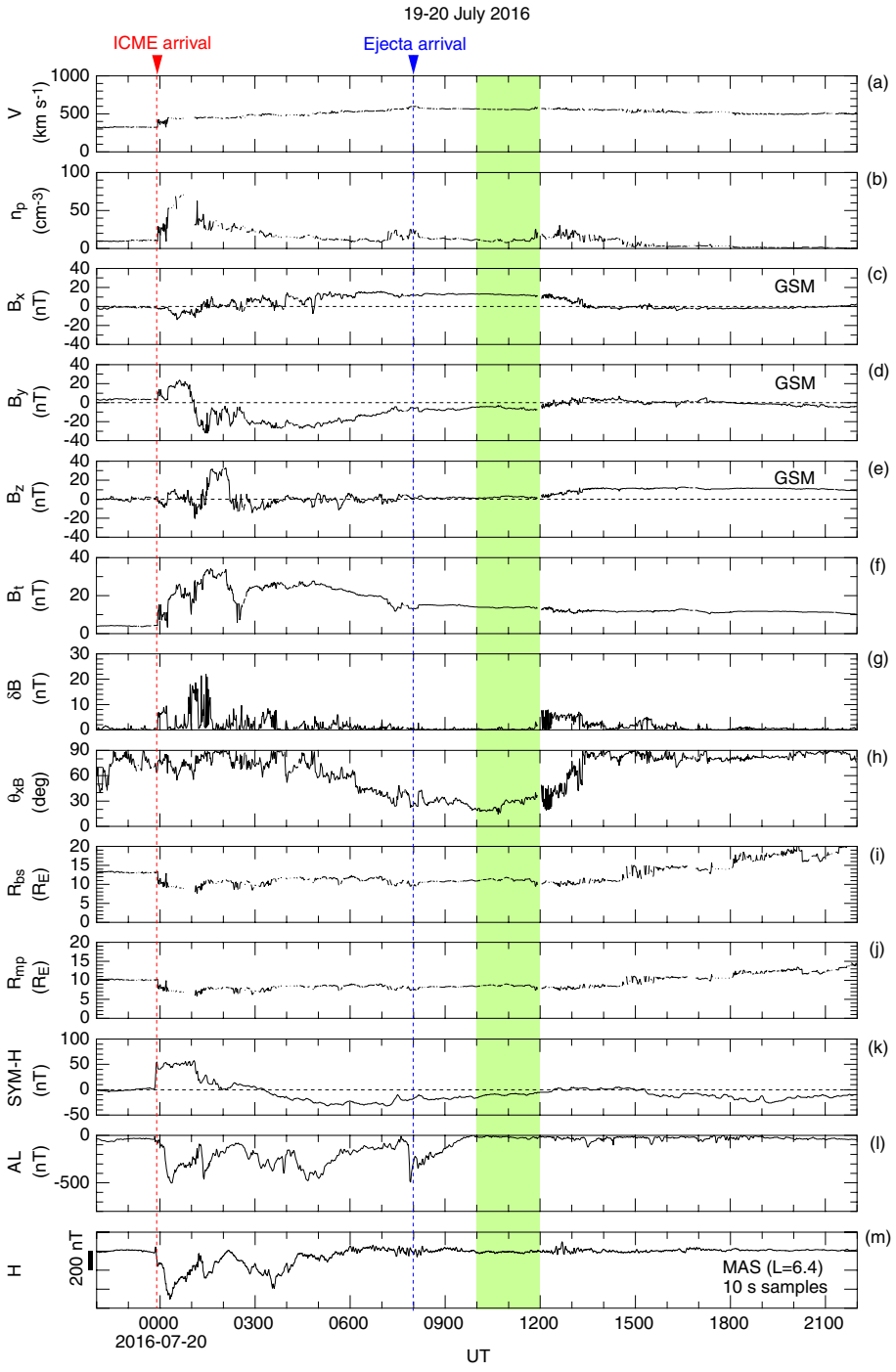

Figure 1. Solar wind parameters (1 min resolution) included in the OMNI data, parameters derived from the data, and geomagnetic data and indices for a 1 day period starting from 2200 UT on July 19, 2016. The red and blue vertical lines indicate the arrival of an ICME and the associated ejecta, respectively. The green shading highlights the 2 h period selected for detailed data analysis. (a) Solar wind velocity. (b) Proton density. (c-f) Components in Geocentric Solar Magnetospheric (GSM) coordinates and magnitude of the magnetic field. (g) Root-mean-square amplitude of the magnetic field computed from the three vector components. (h) Magnetic field cone angle. (i) Bow shock standoff distance according to Farris and Russell (1994). (j) Magnetopause standoff distance according to Shue et al. (1998). (k) SYM-H index. (l) AL index. (m) *H*-component of the magnetic field at the Masi station included in the EMMA. EMMA, European quasi Meridian Magnetometer Array; ICME, interplanetary coronal mass ejection.

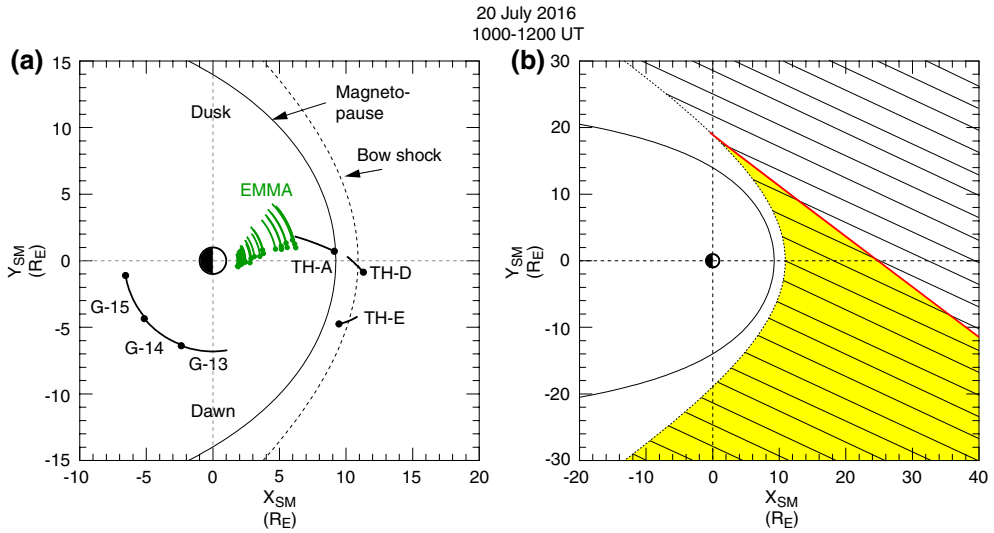

Figure 2. (a) Locations of the THEMIS (TH) and GOES (G) spacecraft and the EMMA stations from 1000 UT to 1200 UT on July 20, 2016, mapped along model magnetic field lines to the equatorial plane of solar magnetic (SM) coordinates. The dots show the locations at 1000 UT. The dashed and solid curves indicate realistic bow shock and magnetopause models described in the text. (b) Schematics of the ion foreshock (shaded yellow) representative of the IMF orientation during the selected 2 h interval. The parallel straight lines indicate the IMF orientation, and the red line indicates the foreshock boundary. EMMA, European quasi Meridian magnetometer array; THEMIS, time history of events and macroscale interactions during substorms; GOES, Geostationary Operational Environmental Satellite; IMF, interplanetary magnetic field.

3.2. Observatory Locations

Figure 2a shows the observatory locations during the selected 2 h interval, projected to the equatorial plane of solar magnetic (SM) coordinates along the field lines of the centered dipole for the spacecraft or International Geomagnetic Reference Field (IGRF) (Bilitza et al., 2017) for the ground stations. Model magnetopause (solid line) and bow shock (dashed line) are included. The boundary shapes are taken from Fairfield (1971) with the standoff distances modified to approximately match the boundary crossings by the spacecraft. THEMIS-D moved from the solar wind (including the foreshock) to the magnetosheath, and THEMIS-E moved from the magnetosheath to the solar wind. THEMIS-A was in the dayside outer magnetosphere, starting close to the magnetopause and moving deeper into the magnetosphere. GOES-13, -14, and -15 were on the nightside. The EMMA stations were near noon in approximate magnetic local time (MLT) conjunction with the THEMIS spacecraft.

Figure 2b shows a schematic illustration of the geometry of the near-Earth space at 1000 UT–1200 UT. The IMF (parallel straight lines) makes a small angle with the Earth-Sun line as shown in Figure 1h, forming an ion foreshock (shaded yellow) sunward of the three THEMIS spacecraft. In this situation, one expects that a large portion of the dayside magnetosphere is filled with ULF waves originating in the foreshock.

3.3. Mass Density Radial Profile

To understand how MHD waves propagate in the magnetosphere, it is necessary to know the plasma mass density there because the density, along with the magnetic field, controls the speed and amplitude of the waves. In particular, we are interested in the location of steep radial density gradients such as the plasmapause and the edges of drainage plumes where fast mode waves may be reflected or trapped (Clausen & Glassmeier, 2014; Hartinger et al., 2010; Takahashi et al., 2010). We have two sources of information on the mass density. The first is the spacecraft potential from the THEMIS spacecraft (Bonnell et al., 2008), and the second is the frequencies of toroidal waves detected on the ground or in space. The spacecraft potential is related to the electron density (Mozer, 1973), but it provides information on mass density structures as well unless the ion composition strongly changes with position.

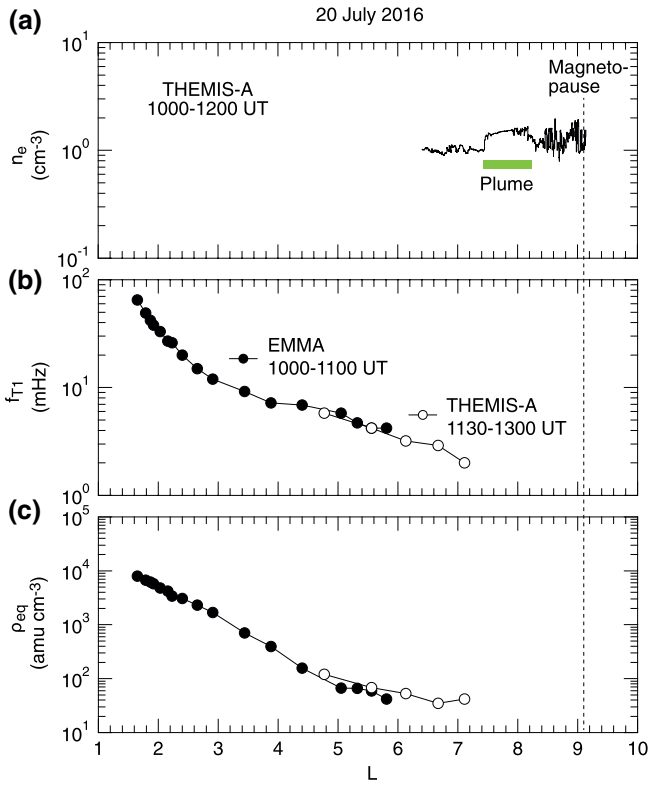

Figure 3. Quantities derived using EMMA or THEMIS-A data and plotted versus L. (a) Electron density at THEMIS-A, derived from the spacecraft potential data for 1000 UT–1200 UT. The green horizontal bar indicates a plasma plume. The vertical dashed line indicates the magnetopause. (b) Fundamental frequency of toroidal standing Alfvén waves detected by EMMA during 1000 UT–1100 UT and by THEMIS-A during 1130 UT–1300 UT. (c) Equatorial mass density corresponding to the fundamental frequency. EMMA, European quasi Meridian magnetometer array.

Figure 3a shows the electron density (n_e) derived from the spacecraft potential measured by THEMIS-A at 1000 UT–1200 UT. At this time, the spacecraft potential was high, and n_e is likely underestimated. What is important is the elevated n_e seen at L~8. For more information on the plasma structure, we inspected the ion energy spectra (McFadden et al., 2008) and the intensity of whistler mode waves (Roux et al., 2008) at the same spacecraft. Based on the presence of enhanced cold (<100 eV) ion fluxes and strong whistler mode emissions (data not shown), we conclude that the spacecraft was in a plasma plume from 1045 UT ($L = 8.2$) to 1125 UT ($L = 7.3$). This time interval corresponds to the green horizontal bar.

Figure 3b shows the frequency of fundamental toroidal waves (f_{T1}) that we use to estimate the mass density. The filled circles indicate near-noon values obtained by applying the cross-phase technique of Waters et al. (1991) to the EMMA data for 1000 UT–1100 UT. The f_{T1} samples cover $L = 1.6$–5.8. The open circles indicate f_{T1} values determined by inspecting the power spectra of azimuthal oscillations of the ion velocity and the magnetic field at THEMIS-A computed in a 20 min moving data window. The THEMIS-A f_{T1} samples cover $L = 4.8$–7.1. In the region of overlap ($L = 4.8$–5.8), the EMMA and THEMIS-A results agree very well.

Figure 3c shows the equatorial mass density (ρ_{eq}) corresponding to the f_{T1} estimates, obtained by numerically solving the Singer et al. (1981) equation for toroidal waves. In solving the equation, we used the Tsyganenko (1989) magnetic field model and assumed that the mass density varies along the field line as r^{-1}, where r is the geocentric distance to the field line. The mass density decreases with L at $L < 7$. The data point at the highest L suggests an outward ρ_{eq} gradient at $L > 7$, which could be the inner edge of the plasma plume noted in the n_e plot.

4. Dayside Spacecraft Observations

This section describes ULF waves observed on the dayside.

4.1. Time Series

Figures 4a–4e show parameters included in or derived using the OMNI data for the 2 h period. In the solar wind, B_t was nearly constant at ~14 nT (Figure 4a). The orientation of the IMF did not change much either, with the cone angle θ_{xB} in the range 14°–40° (Figure 4b), and the clock angle ϕ_{yzB} in the range 275°–308° (Figure 4c). The theoretical foreshock wave frequency f_{fw} is in the range 59 mHz–96 mHz (Figure 4d), which is mostly in the upper half of the Pc3 band (22 mHz–100 mHz). The magnetopause stand-off distance R_{mp} according to the Shue et al. (1998) model is ~8 R_E (Figure 4e).

Figures 4f–4l show THEMIS data. THEMIS-D was initially in the ion foreshock, made two brief entries into the magnetosheath, and, after 1049 UT, remained in the magnetosheath (Figures 4f–4h). The region identification is made using the ion density n_i, which is ~10^2 cm^{-3} in the magnetosheath and ~10 cm^{-3} in the foreshock. The difference between the two regions is also evident in the magnetic field data, that is, B_t is higher and the cone angle is larger in the magnetosheath. THEMIS-E, which was moving outward, was initially in the magnetosheath and moved into the foreshock after multiple boundary crossings (Figures 4i–4k). The density at THEMIS-E is much higher than at THEMIS-D. This is because THEMIS-D was operating in the special mode to detect low-energy particles with much worse energy resolution for the thermal population. THEMIS-A was moving earthward within the magnetosphere, and, as a consequence, B_t at this spacecraft increased with time (Figure 4l). Plasma data (not shown) indicate that the spacecraft was in the low-latitude boundary layer (LLBL) at 1000 UT–1007 UT, but we classify this interval as magnetosphere

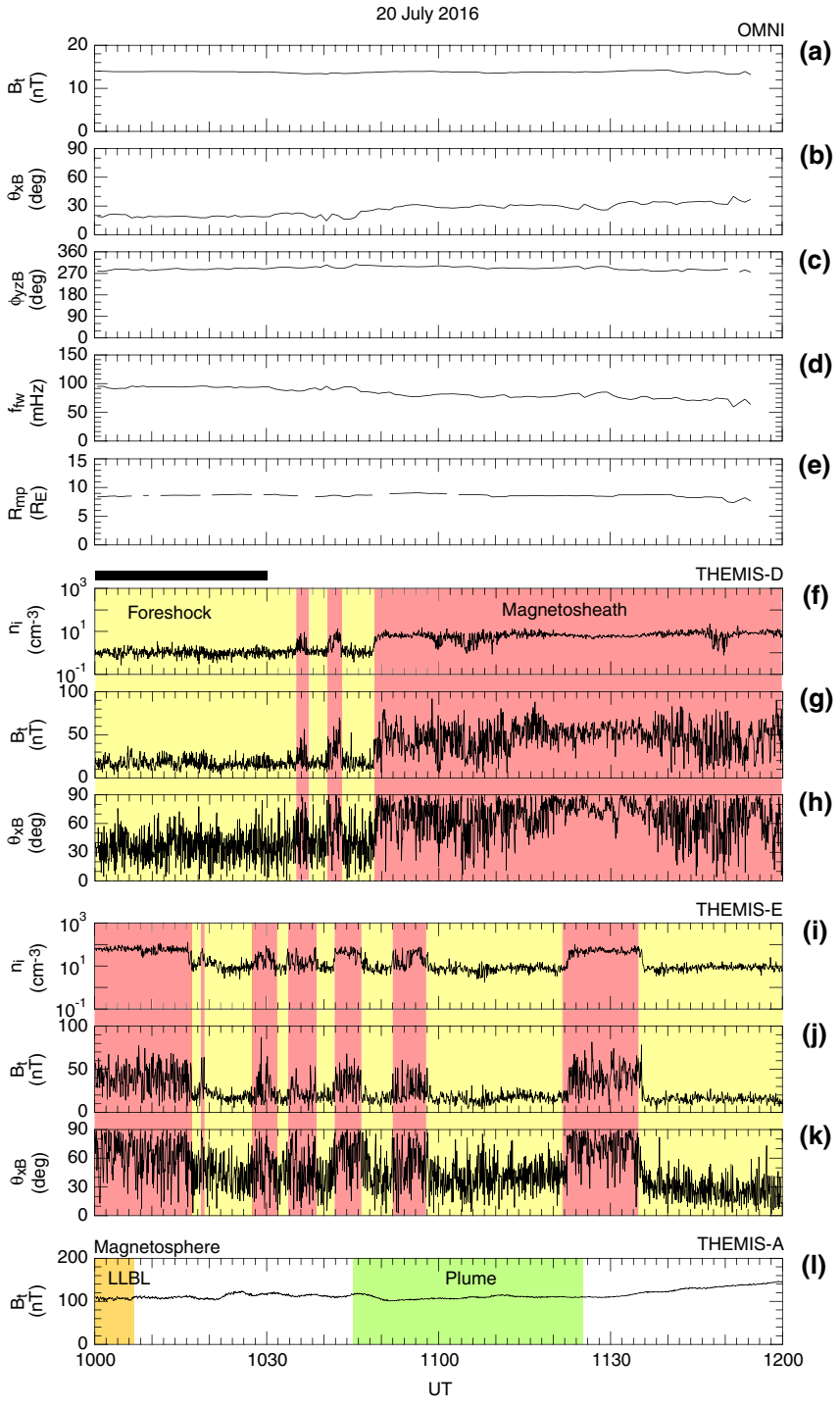

Figure 4. (a-c) Magnitude, cone angle, and clock angle of the IMF defined in GSM coordinates. The source for these parameters is the OMNI data time shifted to the bow shock nose. (d) Frequency of foreshock waves given by Equation 1. (e) Magnetopause stand-off distance according to Shue et al. (1998). (f-h) Ion density, magnetic field magnitude, and the magnetic field cone angle at THEMIS-D, plotted at the time resolution of the spacecraft spin period. The yellow shading indicates the foreshock, and the red shading indicates the magnetosheath. The black bar indicates the 30 min interval selected for detailed analysis. (i-k) Same as (f-h) but for THEMIS-E. (l) Magnetic field magnitude at THEMIS-A. The spacecraft was in the magnetosphere. The orange shading indicates detection of plasma that is characteristic of the low-latitude boundary layer (LLBL). The green shading indicates that the spacecraft was in a plasma plume. IMF, interplanetary magnetic field.

because the magnetic field does not show a sharp change at 1007 UT. The plasma plume interval is shaded green. Slow variations of B_t are seen at this spacecraft, but oscillations of interest to us are not visible with the compressed amplitude scale.

4.2. Dynamic Spectra

Figure 5 is a dynamic display of spectral parameters of the selected field components at the three THEMIS spacecraft. To capture fast mode and other magnetically compressional waves in the foreshock/magnetosheath region covered by THEMIS-D and -E, we show B_t spectra in Figures 5a and 5b. The colored bars at the top indicate whether the spacecraft was in the foreshock (yellow) or the magnetosheath (red). The black bar farther above indicates the 30 min time interval we examine in detail below. To capture magnetospheric fast mode waves at THEMIS-A, we show the power and cross-phase spectra computed from the E_ϕ and B_t components (Figures 5c–5e), where E_ϕ is the electric field component perpendicular to the measured magnetic field and directed eastward. In each panel, we include a line plot of f_{fw} repeated from Figure 4d.

In the foreshock region, the B_t power sometimes exhibits broadband enhancements around f_{fw}. This is evident at 1015 UT–1030 UT (f_{fw}~95 mHz) at THEMIS-D and at 1110 UT–1120 UT (f_{fw}~80 mHz) at THEMIS-E. After the 1137 UT entry into the foreshock, the B_t power at THEMIS-E is low, which may be explained by the gradual increase of the IMF cone angle from ~20° at 1000 UT to ~40° at 1150 UT (Figure 4b). A larger cone angle would mean a weaker foreshock wave intensity at THEMIS-E, which is then located closer to the foreshock edge than earlier during the event (see Figure 2). Near the foreshock edge, the wave power is lower because of the lower suprathermal ion density, which results in a lower growth rate of the foreshock waves (Gary, 1993).

In the magnetosheath, the B_t power is much higher than in the foreshock throughout. There is considerable power below 50 mHz, with peak power sometimes occurring at ~30 mHz, for example, at 1000 UT–1020 UT at THEMIS-E (Figure 5b), and at 1050 UT–1110 UT at THEMIS-D (Figure 5a). Spectral peaks occur at f_{fw}, but they do not stand out as a persistent feature.

In the magnetosphere (THEMIS-A), the power spectra are similar between the E_ϕ and B_t components (Figure 5c and 5d). These spectra indicate that the wave power decreases with increasing frequency faster than in the foreshock or the magnetosheath, giving the impression that the magnetosphere is acting as a low-pass filter to disturbances applied externally. There is an indication that the spectra are enhanced at f_{fw}, most notably at ~1030 UT (~100 mHz). Interestingly, the E_ϕ-B_t cross-phase (Figure 5e) at this instance, and also at 1010 UT and 1050 UT, is near ±180°, reminiscent of a case reported by Takahashi et al. (1994b). This implies that there were tailward-propagating fast mode waves at the predicted foreshock wave frequency. The E_ϕ and B_t spectra show strong oscillations below 50 mHz. However, there is little coherence between E_ϕ and B_t in this frequency domain. The plasma plume (1045 UT–1125 UT, green horizontal bar) does not appear to affect the spectra.

We examined magnetic field variations just outside the magnetosheath using high-time-resolution (0.062 s) data available from THEMIS-E. Figures 6a and 6b show the B_z component in geocentric solar ecliptic (GSE) coordinates and B_t for 1100 UT–1110 UT. Both components exhibit large-amplitude quasiperiodic oscillations with peak-to-peak amplitudes in excess of 20 nT, which is greater than the mean B_t value ~16 nT. The corresponding power spectra (Figure 6d) indicate enhanced power at 80 mHz that is predicted by Equation 1. Spectral enhancements occur at other frequencies as well, indicating that the foreshock wave consists of multiple frequencies. For example, the B_t spectrum is enhanced at 25–45 mHz, which might be related to the magnetosheath B_t power observed in similar bands.

5. Dayside Ground Observations

In this section, we examine dayside magnetic field oscillations on the ground detected by EMMA and how they are related to dayside ULF waves in space. Table 1 indicates the station code, geographic latitude, and longitude, and L value for each EMMA station, where L is defined using the IGRF.

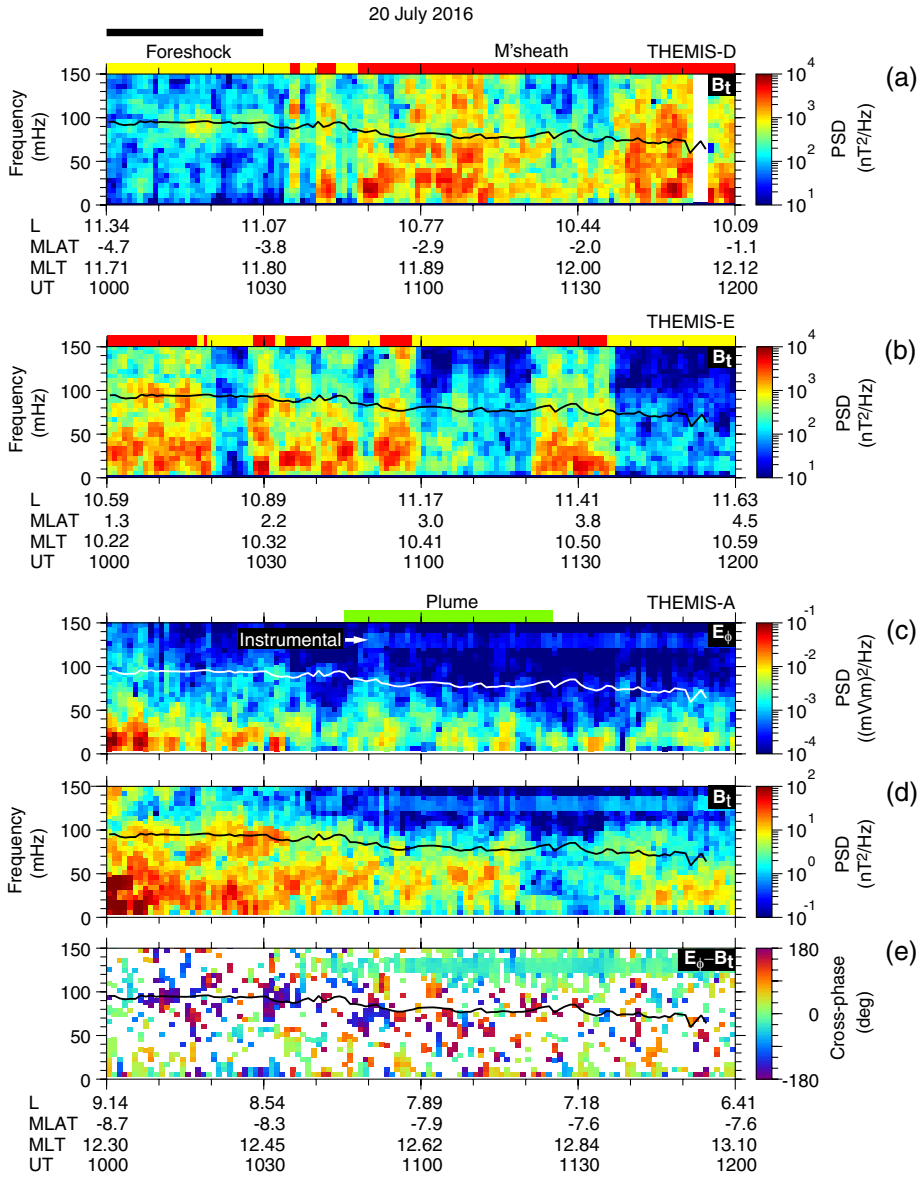

Figure 5. Dynamic display of spectral parameters. (a) Power spectral density (PSD) of B_t at THEMIS-D. The spacecraft was located in the ion foreshock or in the magnetosheath. The superimposed line plot indicates the theoretical foreshock wave frequency f_{fw}. The yellow and red bars at the top indicate foreshock and magnetosheath intervals, respectively. The black horizontal bar indicates the 30 min interval selected for detailed analysis. MLAT is dipole magnetic latitude in degrees. (b) Same as (a) but for THEMIS-E. (c) PSD of E_ϕ at THEMIS-A. The spacecraft was located in the magnetosphere. The green horizontal bar indicates the spacecraft encounter with a plasma plume. The stable spectral line at 130 mHz is instrumental. (d) Same as (c) but for B_t. (e) Cross-phase between E_ϕ and B_t, shown if the E_ϕ-B_t coherence is > 0.5.

5.1. *L* Dependence

Figure 7 shows time series and spectra of magnetic field oscillations at 1000 UT–1030 UT. We selected this interval because three spacecraft made simultaneous observations in different regions: the foreshock (THEMIS-D), magnetosheath (THEMIS-E), and magnetosphere (THEMIS-A). The selected time interval is marked by a black horizontal bar in Figures 4 and 5. Fortuitously, the MLT separation between THEMIS-A and EMMA was very small. The B_t time series in the foreshock (Figure 7a), magnetosheath (1000 UT–1017 UT, Figure 7b), and magnetosphere (Figure 7c) exhibits irregular oscillations, with the amplitude being the largest in the magnetosheath and smallest in the magnetosphere.

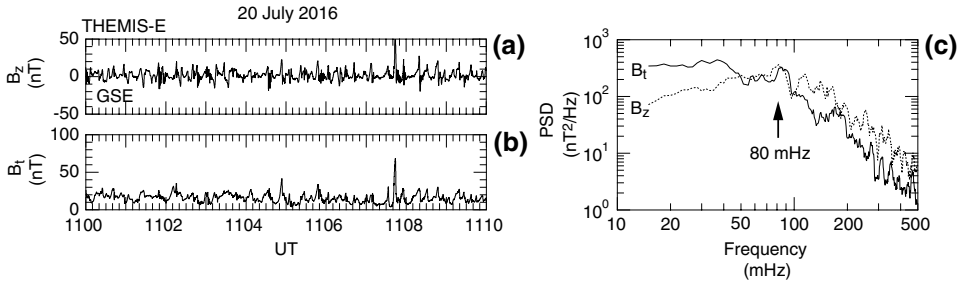

Figure 6. (a, b) Magnetic field GSE z component (B_z) and magnitude B_t at THEMIS-E, plotted at 0.062-s time resolution. (c) Power spectra computed from the time series data shown in panels (a) and (b). The arrow indicates the theoretical foreshock wave frequency given by Equation 1 for $B_t = 14$ nT and $\theta_{xB} = 29°$ according to the OMNI data shown in Figure 4. GSE, geocentric solar ecliptic.

On the ground, oscillations are also present in both H (Figure 7d) and D (Figure 7e). The H waveform changes with L. For example, a wave packet seen at ~1007 UT at $L < 2$ is not obvious at $L > 2$. The H amplitude becomes smaller at lower L, although oscillations are still visible at the lowest L. The D component behaves differently. The D waveform changes little with L, but the D amplitude diminishes as L decreases. D oscillations are hardly visible at $L < 2$ with the given amplitude scale. These observations imply that fast mode waves contribute to H oscillations near the magnetic equator (Allan et al., 1996) and that the D oscillations are related to the azimuthal tilt of the magnetic field lines at the ionospheric level that is induced by field line oscillations symmetric about the magnetic equator (Sugiura & Wilson, 1964).

Table 1
European quasi Meridian Magnetometer Array magnetometer sites

Location	Code	Latitude (°)	Longitude (°)	L
Kevo	KEV	69.76	27.01	6.51
Masi	MAS	69.46	23.70	6.41
Kilpisjärvi	KIL	69.06	20.77	6.26
Ivalo	IVA	68.56	27.29	5.91
Muonio	MUO	68.02	23.53	5.72
Sodankylä	SOD	67.37	26.63	5.40
Pello	PEL	66.90	24.08	5.25
Ranua	RAN	65.90	26.41	4.86
Mekrijärvi	MEK	62.77	30.97	3.94
Hankasalmi	HAN	62.25	26.60	3.83
Nurmijärvi	NUR	60.50	24.65	3.46
Tartu	TAR	58.26	26.46	3.06
Birzai	BRZ	56.21	24.75	2.76
Hel	HLP	54.61	18.81	2.55
Belsk	BEL	51.83	20.80	2.25
Polesie	PPN	51.44	23.13	2.21
Zagorzyce	ZAG	50.28	20.58	2.11
Vyhne	VYH	48.49	18.84	1.96
Nagycenk	NCK	47.63	16.72	1.89
Tihany	THY	46.90	17.89	1.84
LonskoPolje	LOP	45.32	16.78	1.74
Ranchio	RNC	43.97	12.08	1.65
L'Aquila	AQU	42.38	13.32	1.57

The power spectra calculated from the time series data are shown in the right column of Figure 7. The ion foreshock spectrum (Figure 7f) shows a broad peak centered at ~90 mHz, which is not far from the theoretical frequency 94 mHz (vertical dashed line). In addition, there is a peak at 24 mHz. The magnetosheath spectrum (Figure 7g) has some similarity to the foreshock spectrum with a bump at ~90 mHz. However, the spectrum is also peaked at 12, 35, and 54 mHz. The magnetosphere spectrum (Figure 7h) shows a peak at 94 mHz, but this peak is minor compared to the peaks at 12 and 40 mHz. To briefly summarize, spectral power is enhanced at or near f_{fw} in all three regions, but the power level at this frequency is lower than that at the lower-frequency peaks.

The EMMA H spectra (Figure 7i), which cover the Pc2–Pc4 bands in full, generally differ from those in space. We find a few prominent features in the H spectra. First, there is a 10 mHz enhancement from $L = 1.74$ (LOP) to $L = 3.83$ (HAN), which is marked by a red dashed line. At some stations (e.g., NUR), this is the strongest oscillation, with a peak-to-peak amplitude reaching 6 nT, as marked by black triangles above the NUR time series in Figure 7d. The oscillation is reminiscent of an 11 mHz cavity mode oscillation reported by Takahashi et al. (2010) during a period of low IMF cone angle. In the present example, the foreshock waves had spectral power centered well above 10 mHz, and neither the magnetosheath (Figure 7g) nor the outer magnetosphere (Figure 7h) spectrum exhibits a peak at 10 mHz.

Second, we see a peak starting at 17 mHz at HLP ($L = 2.55$) and moving to higher frequencies as L decreases, reaching 70 mHz at AQU ($L = 1.6$). We attribute the peak to the fundamental toroidal (T1) wave, which we presented in Figure 3. T1 wave signals can be extracted at $L > 2.5$ by the cross-phase technique, but they are not visible in Figure 7i because they

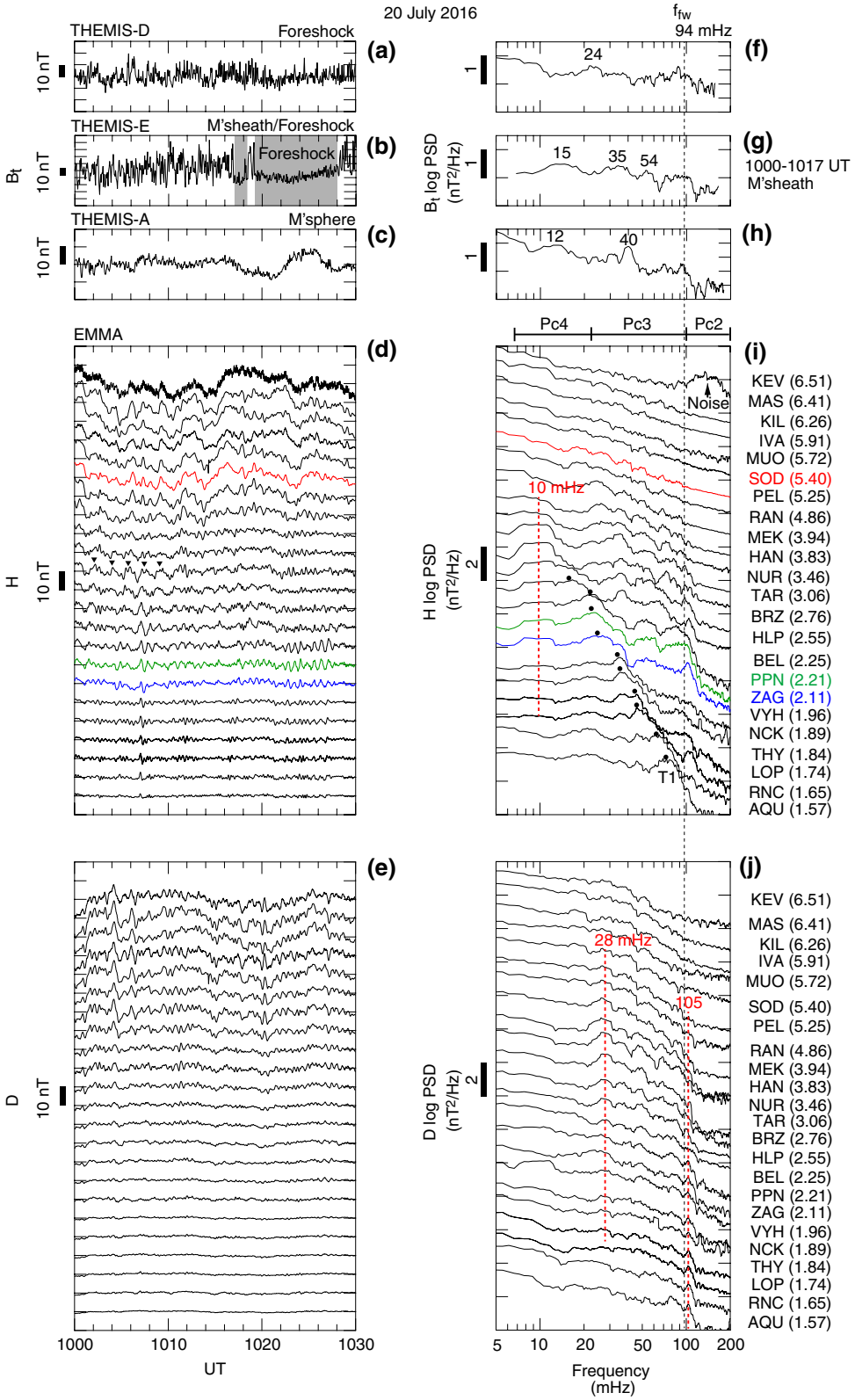
20 July 2016
THEMIS-D
Foreshock
(a)
10 nT
THEMIS-E
M'sheath/Foreshock
Foreshock
(b)
Bt
10 nT
THEMIS-A
M'sphere
(c)
10 nT
EMMA
(d)
H
10 nT
(e)
D
10 nT
1000
1010
1020
1030
UT
ffw
94 mHz
(f)
24
1
(g)
15
35
54
Bt log PSD
(nT²/Hz)
1
1000-1017 UT
M'sheath
(h)
12
40
1
Pc4
Pc3
Pc2
(i)
Noise
10 mHz
H log PSD
(nT²/Hz)
2
T1
KEV (6.51)
MAS (6.41)
KIL (6.26)
IVA (5.91)
MUO (5.72)
SOD (5.40)
PEL (5.25)
RAN (4.86)
MEK (3.94)
HAN (3.83)
NUR (3.46)
TAR (3.06)
BRZ (2.76)
HLP (2.55)
BEL (2.25)
PPN (2.21)
ZAG (2.11)
VYH (1.96)
NCK (1.89)
THY (1.84)
LOP (1.74)
RNC (1.65)
AQU (1.57)
(j)
28 mHz
105
D log PSD
(nT²/Hz)
2
KEV (6.51)
MAS (6.41)
KIL (6.26)
IVA (5.91)
MUO (5.72)
SOD (5.40)
PEL (5.25)
RAN (4.86)
MEK (3.94)
HAN (3.83)
NUR (3.46)
TAR (3.06)
BRZ (2.76)
HLP (2.55)
BEL (2.25)
PPN (2.21)
ZAG (2.11)
VYH (1.96)
NCK (1.89)
THY (1.84)
LOP (1.74)
RNC (1.65)
AQU (1.57)
5
10
20
50
100
200
Frequency
(mHz)

are masked by the strong 10 mHz oscillation. Other peaks occur at frequencies that change with L. These could be the manifestation of higher harmonics of the toroidal wave.

Third and most important, we do not find any outstanding spectral peak in the H component at multiple ground stations at the theoretical foreshock wave frequency. This is a significant departure from the case reported by Clausen et al. (2009), as we discuss in Section 8.

The EMMA D spectra (Figure 7j) are quite different from the H spectra. The spectral shape does not change much with L, and there is no indication of the local T1 oscillations. Notable features are a peak at 28 mHz appearing at $L = 3.0-5.4$ and a peak at 105 mHz appearing below $L = 2.5$. The second frequency is not very far from f_{fw} and might be the result of transmission of foreshock waves into the deep part of the plasmasphere. Still, the spectral intensity at 105 mHz is very modest, and one would barely notice this component in time series plots.

5.2. Relation to Magnetospheric ULF Waves

Although the intensity of ground pulsations was elevated during the passage of the magnetic cloud, we find little coherence between compressional waves in the magnetosphere and pulsations on the ground. Figure 8 shows dynamic power spectra and cross-spectra computed from the B_t component at THEMIS-A and the H component at SOD ($L = 5.4$) and PPN ($L = 2.2$). THEMIS-A was on an inbound leg with its L changing from 9.14 at 1000 UT to 6.41 at 1200 UT. The MLT separation between the spacecraft and ground stations was less than 2 h.

The dynamic spectra show little resemblance between space and ground. The THEMIS-A spectra (Figure 8a) exhibit a broadband nature of ULF waves with significant intensity variations that can be either spatial or temporal. The observed general decrease of the power with time would be consistent with attenuation of waves as the spacecraft moves away from the magnetopause. At SOD (Figure 8b), the power is intense below 50 mHz, and there is no peak at ~100 mHz. At PPN, the power is peaked at 25 mHz and 90 mHz (Figure 8c), which are attributed to the T1 and T3 modes (see Figure 10). The dynamic cross-spectra (Figures 8d and 8e) confirm low coherence between space and ground. A similar result has been obtained for a Pc3 event observed at L~6 by Active Magnetospheric Particle Tracer Explorers/Charge Composition Explorer (AMPTE), and at a geomagnetically conjugate ground station even when power spectra are similar between space and ground (Takahashi et al., 1994a).

To gain more insight into the space-ground relationship, we generated EMMA grams (Takahashi & Heilig, 2019). EMMA grams display high-pass filtered magnetic field time series from many (23 in the present study) stations as two-dimensional (2-D) images in the time versus L space. The main advantage of this format over conventional stacked line plots is that the pixel L boundaries are placed at the midpoints of neighboring stations so that the images appear uniform in L. This makes visual identification and interpretation of spatio-temporal structures of magnetic pulsations straightforward. Figures 9b and 9c show EMMA grams generated for 1000 UT–1015 UT. Filtering is done by subtracting 21 s running averages from the original time series. The B_t data from THEMIS-A are also high-pass filtered and displayed in Figure 9a. An expanded 5-min segment of the image for $L < 4$ is displayed in Figures 9e and 9f along with the corresponding B_t line plot (Figure 9d).

The H EMMAgrams exhibit numerous stripes with a slight tilt or slope equivalent to poleward motion of pulses or phase fronts. The degree of tilt varies with L, with larger tilt appearing mainly at $L < 2.5$ (see Figure 9e). Takahashi and Heilig (2019) noted that poleward propagating patterns can arise from field line

Figure 7. (a-c) Detrended B_t components at THEMIS-D (ion foreshock), THEMIS-E (magnetosheath or foreshock), and THEMIS-A (magnetosphere). The time resolution of the data is 3.2 s for THEMIS-D, 3.0 s for THEMIS-E, and 2.8 s for THEMIS-A. (d, e) Detrended H and D components at the EMMA stations. The H component at KEV is contaminated by broadband noise. The H data from SOD, PPN, and ZAG are colored for comparison with other figures showing data from these stations. The black triangles are placed at the peaks of 100 s oscillation seen in the H component at NUR. (f-j) Power spectra computed from the time series data shown in the left column. The THEMIS-E spectrum is computed using the magnetosheath interval 1000 UT–1017 UT. The EMMA station code is shown on the right with the L values given in parentheses. The black vertical dashed line indicates the theoretical foreshock wave frequency. The black dots in panel (i) indicate fundamental toroidal wave frequencies. The red vertical dashed lines in panels (i) and (j) indicate spectral peaks occurring at multiple stations. EMMA, European quasi-Meridian magnetometer array.

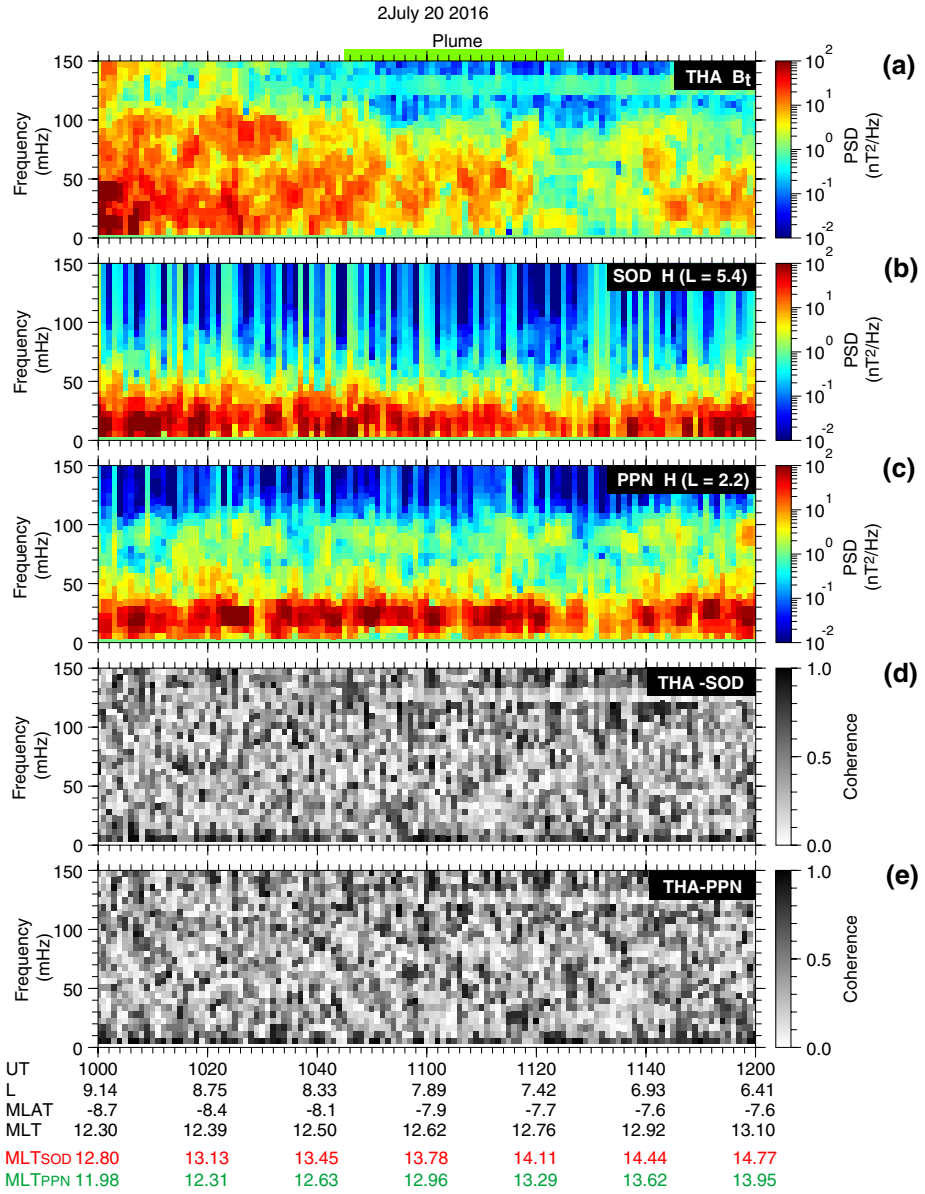

Figure 8. (a) Dynamic spectra of the B_t component at THEMIS-A, the same as Figure 5d but with a different dynamic range. (b), (c) Dynamic spectra of the H component at the EMMA stations SOD and PPN. (d), (e) Coherence between B_t and H. The location of the spacecraft is shown at the bottom in black. The MLT values of the ground stations are shown in red (SOD) and green (PPN). EMMA, European quasi-Meridian magnetometer array; MLT, magnetic local time.

resonance driven by monochromatic driver waves, eigenmode oscillation of field lines at L-dependent frequency (transient pulsations), or the travel time effect proposed by Tamao (1964). During transient pulsations, the tilt of the ridges (stripes) seen in the time-L plane increases with time (Poulter & Nielsen, 1982), whereas the other two maintain a constant tilt.

Transient pulsations appear to account for the majority of magnetic pulsations at low latitudes ($L < 3$) in the present example. Large amplitude stepwise increases of the solar wind dynamic pressure (sudden impulses or sudden commencements) excite classical transient pulsations (Petrinec et al., 1996). However, Takahashi and Heilig (2019) revealed that transient pulsations are excited even in the absence of strong solar wind dynamic pressure pulses, which is true in the observations presented here.

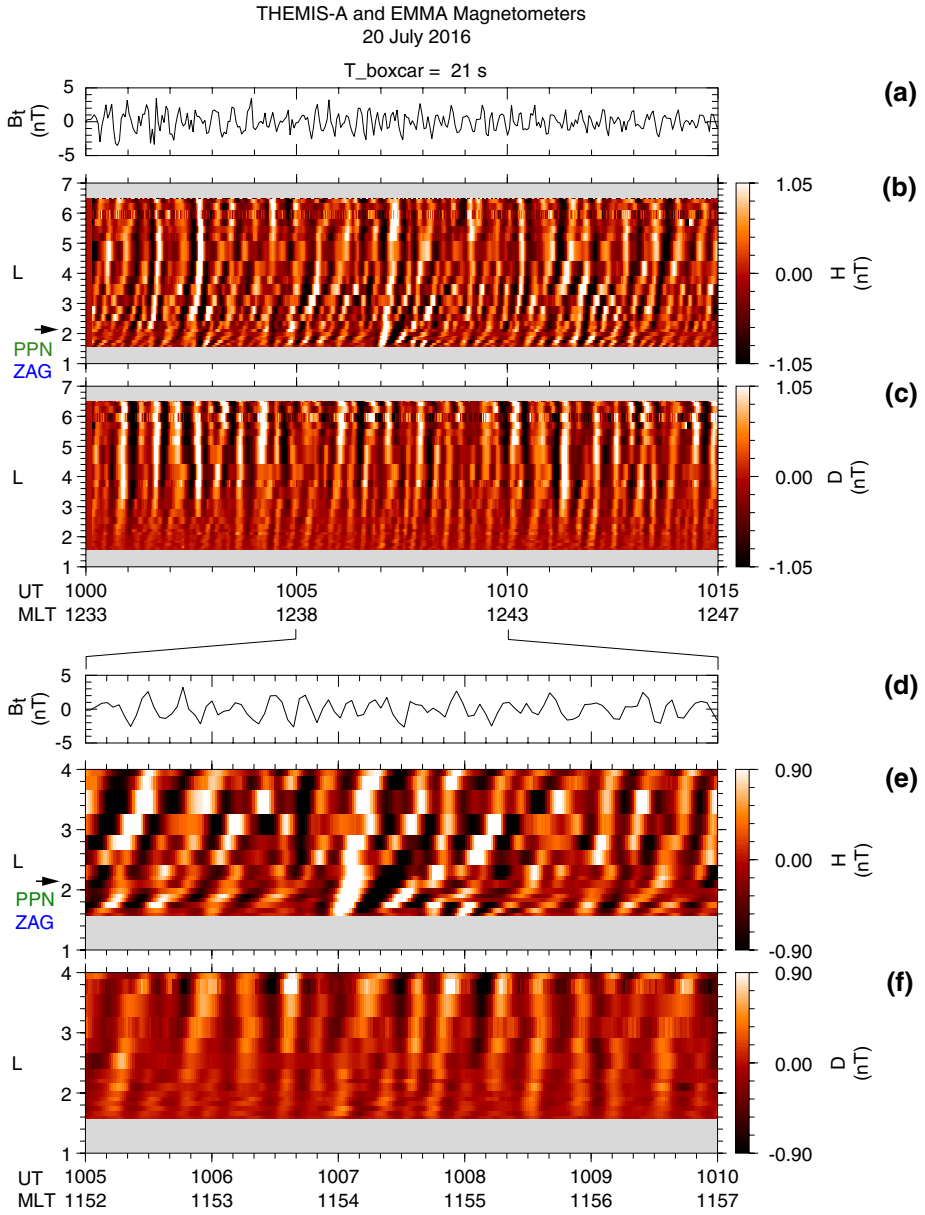

Figure 9. (a) Perturbation of B_t at THEMIS-A about its 21-s running mean. (b, c) EMMAgram (Takahashi & Heilig, 2019) for 1000 UT–1015 UT. The black arrow indicates the midpoint L between PPN and ZAG. (d)-(f) Same as (c) but for a shorter time interval and for $L < 4$.

In Figures 9d and 9e, we find that B_t and H exhibit similar periodicities but cannot unambiguously associate individual peaks between B_t and H. This explains the low space-ground coherence shown in Figure 8. Our interpretation of this time series mismatch is that multiple wave packets are generated in the foreshock and that they impact the magnetosphere more or less independently. The fast mode waves that result from these source waves will propagate in the magnetosphere along different paths, and what a spacecraft or a ground magnetometer detects will be a superposition of these waves. In this situation, we expect the space-ground coherence to be low unless measurements are made very close to each other in L and MLT so that Alfvén waves generated by mode coupling with the fast mode waves and propagating along the magnetic field lines (Tamao, 1964) are detected on the ground with waveforms similar to those of the fast mode waves in space. The spacecraft motion would not change the waveform or spectra at

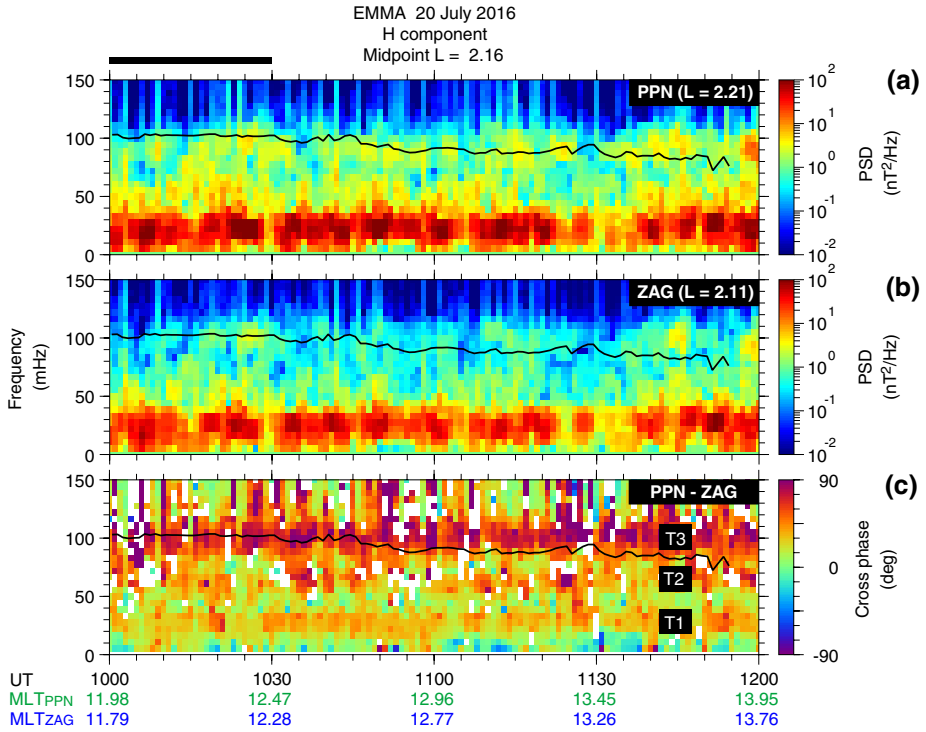

Figure 10. (a) Dynamic spectra of H at the EMMA Polesie (PPN) station. The superimposed line plot indicates f_{fw} given by Equation 1. The black bar indicates the 30 min interval selected for detailed analysis. (b) Dynamic spectra of H at the EMMA Zagorzyce (ZAG) station. (c) Dynamic display of the cross-phase between the H data from PPN and ZAG. EMMA, European quasi-Meridian magnetometer array.

THEMIS-A through the Doppler effect because the fast mode speed is much higher than the spacecraft speed.

Stripes are also visible in the D EMMA grams (Figures 9c and 9f) with signatures of poleward propagation. However, transient pulsations are not found in this component. This is reasonable because transient pulsations are toroidal mode standing Alfvén waves in the magnetosphere, with B_ϕ being the dominant component. The ionospheric screening effect (Hughes & Southwood, 1976) rotates the polarization axis of the Alfvén waves by 90° and produces H-component pulsations on the ground.

5.3. Dynamic Cross-Phase Spectra at $L = 2$

Takahashi and Heilig (2019) argued that transient pulsations give rise to the cross-phase signature reported by Waters et al. (1991). The signature is usually attributed to field line resonance and is fundamental to magnetoseismic studies, which estimate the plasma mass density from the frequencies of observed toroidal waves (Del Corpo et al., 2019). The same argument can be made of the present wave event. Figure 10 shows dynamic spectra computed using data from PPN and ZAG, located near $L = 2$. At PPN (Figure 10a), there is strong spectral power in the 10 mHz–40 mHz band throughout the interval. A secondary enhancement is visible at 80–110 mHz, which covers the theoretical foreshock wave frequency (black line). These spectral features are also evident at ZAG (Figure 10b) but with slightly lower intensities.

The cross-phase spectrum (Figure 10c) shows three bands occupied by cross-phase peaks. The bands are centered at ~30 mHz, ~60 mHz, and ~100 mHz. These are attributed to the T1, T2, and T3 waves. Detection of higher harmonics is not uncommon at low-latitude EMMA stations (Del Corpo et al., 2019). In this example, it appears that strong external disturbances with spectral power extending to ~110 mHz excited strong T3 waves. Despite the clear signature of the T2 mode in the cross-phase spectra, spectral peaks at the T2 frequency are hardly visible in the H spectra at either station. External disturbances having symmetric field

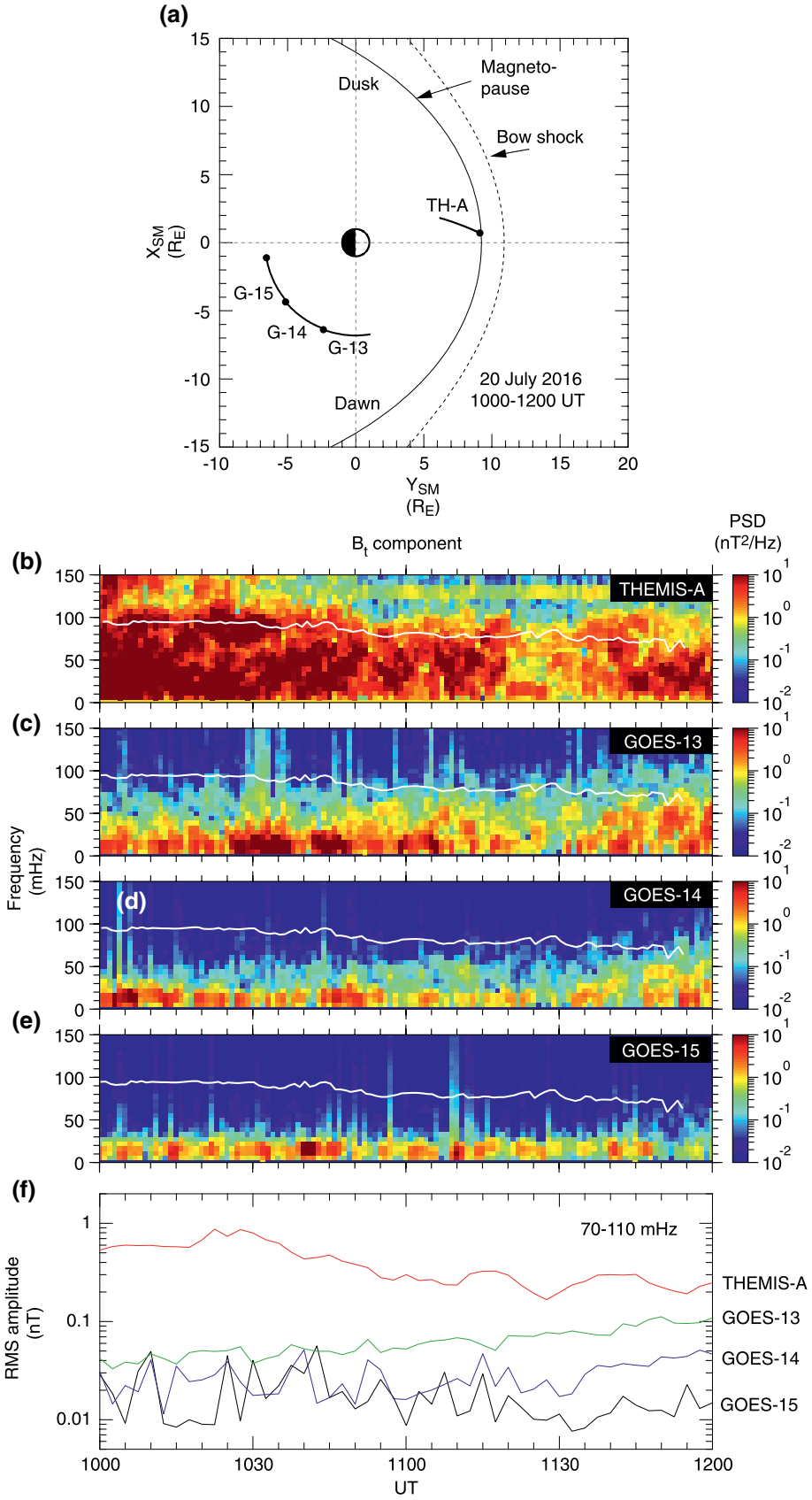
(a)
Dusk
Magneto-
pause
Bow shock
TH-A
G-15
G-14
G-13
Dawn
20 July 2016
1000-1200 UT
X_{SM} (R_E)
Y_{SM} (R_E)
B_t component
PSD
(nT^2/Hz)
(b)
THEMIS-A
(c)
GOES-13
(d)
GOES-14
(e)
GOES-15
Frequency
(mHz)
(f)
70-110 mHz
RMS amplitude
(nT)
THEMIS-A
GOES-13
GOES-14
GOES-15
UT

line displacement about the magnetic equator explain the weak T2 waves, which have an antisymmetric mode structure (Sugiura & Wilson, 1964).

6. Night-side Spacecraft Observations

We examine whether ULF waves of foreshock origin can be detected in the midnight sector, motivated by a study (Takahashi et al., 2016) that reported a clear case of the propagation during a time interval without a magnetic cloud in the solar wind. In that study, fast mode waves were simultaneously detected in the 20–40 mHz band both on the dayside and on the nightside. Figure 11a shows that we have four spacecraft at locations similar to those in the Takahashi et al. (2016) study. Figures 11b–11g show the dynamic spectra computed from the B_t components at the spacecraft. The THEMIS-A spectra are repeated from Figure 5c but with a different dynamic range.

The power spectra strongly depend on the spacecraft position. As expected, the spectra in the noon sector (THEMIS-A) exhibit much higher power than those away from noon. Among the geostationary satellites, GOES-15 shows the lowest power, which is not surprising because this spacecraft was in the midnight sector. Spectral peaks are largely absent near f_{fw} except at THEMIS-A during 1010 UT–1040 UT. These features imply strong attenuation of fast mode waves as they propagate from the dayside to the nightside.

Figure 11f shows the root-mean-square amplitudes of the B_t oscillations in the 70–110 mHz band, that is, around the f_{fw}. We obtained the amplitudes by taking the square root of the band integral of the B_t spectra calculated using a 10 min data window. The amplitude is largest at THEMIS-A and smallest at GOES-15, as was already noted in the dynamic spectra. Between THEMIS-A and GOES-15, the amplitude differs by more than one order of magnitude (two orders of magnitude in spectral power). By comparison, the event reported by Takahashi et al. (2016) exhibited comparable power between day and night.

7. Vlasiator Simulation

Spacecraft observations are complemented with numerical simulations performed with the hybrid-Vlasov model Vlasiator (Palmroth et al., 2018; von Alfthan et al., 2014). This model is designed to carry out global simulations of near-Earth space which include self-consistent ion kinetic physics. It is thus well suited for the present study, which investigates the transmission of waves generated through ion kinetic processes from the upstream foreshock region into the magnetosphere. In the hybrid-Vlasov approach, electrons are treated as a massless charge-neutralizing fluid, whereas ions are modeled as velocity distribution functions whose evolution is dictated by Vlasov's equation. The set of equations is completed with Ampère's and Faraday's laws and the generalized Ohm's law, with the Hall term included.

The velocity distribution functions are represented in a 3-D Cartesian velocity space that is self-consistently coupled with each ordinary space grid cell of the simulation domain. The simulation run presented in this paper is 2-D in ordinary space, corresponding to the equatorial plane of near-Earth space. In Vlasiator, the full strength of Earth's dipole is used, as well as realistic proton charge and mass. As a result, processes are modeled at realistic temporal and spatial scales and are thus directly comparable with spacecraft observations, without further rescaling.

7.1. Simulation Setup

We perform a Vlasiator run with upstream conditions comparable to those encountered at Earth during the interval under study. Because the solar wind parameters were remarkably steady between 0800 and 1200 UT on July 20, 2016, we use the OMNI plasma and IMF parameters averaged over this time interval as inputs to the simulation. The solar wind density is $n = 12$ cm^{-3}, its velocity $V = (-565, 0, 0)$ km s^{-1}, and the IMF vector $B = (12.5, -6.5, 0)$ nT. All vector quantities are given in GSE coordinates. The simulation domain covers the equatorial plane of near-Earth space (GSE X-Y plane), extending from about -8 R_E to 76 R_E along X and from

Figure 11. (a) Locations of spacecraft in the magnetosphere at 1000 UT–1200 UT. (b-e) Dynamic spectra of the B_t components at the spacecraft. The line plot in each panel indicates the foreshock wave frequency given by Equation 1. (f) Root-mean-square (RMS) amplitudes of B_t oscillations in the 70 mHz–110 mHz band.

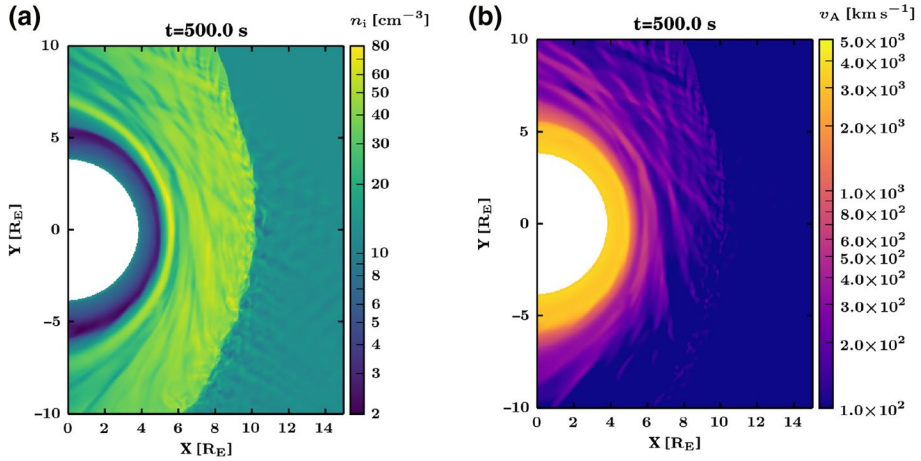

Figure 12. Equatorial snapshots of plasma quantities in the simulation. (a) Proton density. (b) Alfvén velocity.

−60 R_E to 31 R_E along Y. The solar wind flows in from the $+X$ boundary. The inner boundary is a perfectly conducting circle at 25,000 km (3.9 R_E) from Earth's center. The simulation was run for 598 s.

The resolution in velocity space is 30 km s^{-1}, while the spatial resolution is 260 km, which is about 4 times the ion inertial length in the solar wind. As shown in previous studies using Vlasiator, ion kinetic effects arise in the simulation even when the ion inertial length is not resolved, and lead to realistic foreshock dynamics (e.g., Pfau-Kempf et al., 2018; Turc et al., 2018). The foreshock waves of interest here have a wavelength of the order of 1 R_E, which is much larger than the grid resolution. They are properly resolved in the simulation and their properties are in excellent agreement with spacecraft observations in the Earth's foreshock (Palmroth et al., 2015; Turc et al., 2018, 2019).

Though desirable, a 3-D Vlasiator run with the same parameters as presented here is unfortunately not achievable at this time. The transition from 2-D to 3-D is not just a simple matter of extending the grid into a third spatial dimension, because no current supercomputer is large enough to accommodate a 3-D Vlasiator run without downgrading significantly the grid resolution. Extensive code development, such as including adaptive mesh refinement to the model and implementing more efficient solvers, are required before transitioning to 3-D runs, and are currently underway. The present work will serve as a benchmark for Vlasiator 3-D runs once they become available.

7.2. Plasma Domain Configuration

We first describe the global plasma structures in the X-Y plane obtained by the simulation. Figure 12a shows the proton density distribution 500 s after the start of the simulation. The bow shock is visible as the boundary between the low-density solar wind and the high-density magnetosheath, with a standoff distance of ∼10 R_E geocentric. The distance is slightly shorter than the observation (∼11 R_E). The exact magnetopause location is more challenging to determine. Its standoff distance in any given simulation, even in 3-D, varies by several Earth radii depending on which parameter is used for its identification (e.g., Palmroth et al., 2003). Based on the proton density profile shown in Figure 12a, and on the velocity streamlines in Figure 14 a, we place the magnetopause between X∼5.5 R_E and X∼6 R_E. The magnetopause in our run is located much closer to Earth than predicted by the Shue et al. (1998) model (see Figure 1j) and observed by the THEMIS-A spacecraft, which crosses the subsolar magnetopause around $X = 8.2$ R_E at 09:49 UT (not shown). This discrepancy is most likely due to the 2-D setup of our simulation, which results in the IMF lines piling up in front of the magnetopause. The magnetopause is probably pushed earthward by the enhanced magnetic pressure. This effect is more prominent here than in other Vlasiator runs because of the large IMF magnitude. As a result, the magnetosheath thickness is larger in our simulation (4 R_E−4.5 R_E) than observed during 2016-07-20 event (∼3 R_E, see Figure 2).

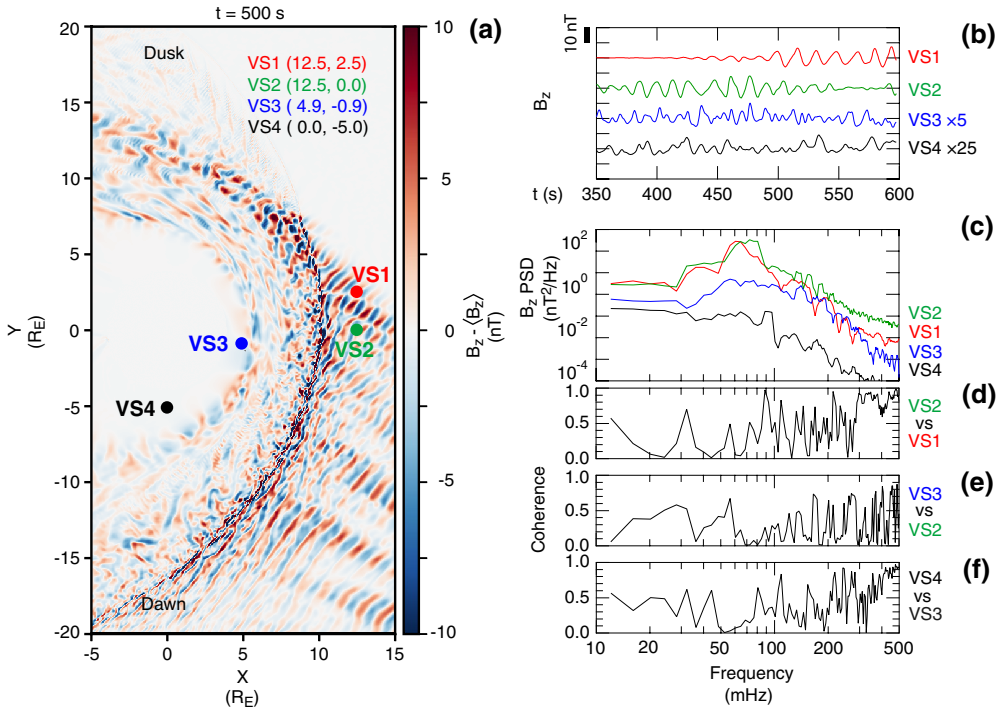

Figure 13. Properties of simulated ULF waves. (a) Snapshot of the perturbation of the magnetic field z component B_z in the X-Y plane. The perturbation is defined relative to the 50-s average $\langle B_z \rangle$ and is evaluated at 500 s into the simulation. (b) Time series plots of B_z at the four virtual spacecraft (VS1, VS2, VS3, and VS4) shown in panel (a). Each trace indicates the unfiltered time series with the baseline adjusted for visual comparison with other traces. The amplitude is magnified by a factor of 5 for VS3 and 25 for VS4. (c) Power spectra of the B_z time series shown in panel (b). (d)-(f) Coherence spectra calculated for three pairs of virtual spacecraft. ULF, ultralow-frequency.

The bow shock is not clear in the Alfvén velocity (V_A) distribution (Figure 12b). This is because the velocity does not change much across the boundary, especially if the shock is quasi parallel (the $Y < 0$ region in this run). However, in the same figure, the magnetopause is clearly visible as a sharp transition from a high-velocity region (orange, magnetosphere) to a low-velocity region (purple, magnetosheath). Within the magnetosphere, V_A is of the order of 2,000–3,000 km s^{-1}. This velocity is much higher than that in the real magnetosphere estimated at THEMIS-A. Using the equatorial mass density shown in Figure 3c and the magnitude of the magnetic field measured by the spacecraft, we find VA∼500 km s^{-1} between 1130 UT ($L = 7.2$) and 1300 UT ($L = 4.6$). The large difference between the simulation and the observation can be explained by the fact that the simulation does not take into account ions that originate from the ionosphere. Because the transmission rate of MHD waves across the magnetopause depends on the wave velocities on both sides of the boundary (McKenzie, 1970), the high velocity would mean that the amplitude of the waves in the magnetosphere is not very realistic. However, because the shape of the magnetopause is realistic, the simulation is useful in understanding the geometric effects on wave propagation in the magnetosphere as we will discuss in Sections 7.3 and 8.3.

7.3. Wave Properties

An important question we address using the simulation is the spatial variation of wave fields. Figure 13 shows an example of analysis we have done on the global properties of the simulated ULF waves. As stated in the introduction, foreshock waves generate fast mode waves in the magnetosphere, which then couple to eigenmode oscillations of the magnetospheric field lines. The latter cannot develop in the simulation, because field line resonances would require a 3-D setup in ordinary space. Therefore, in the simulation,

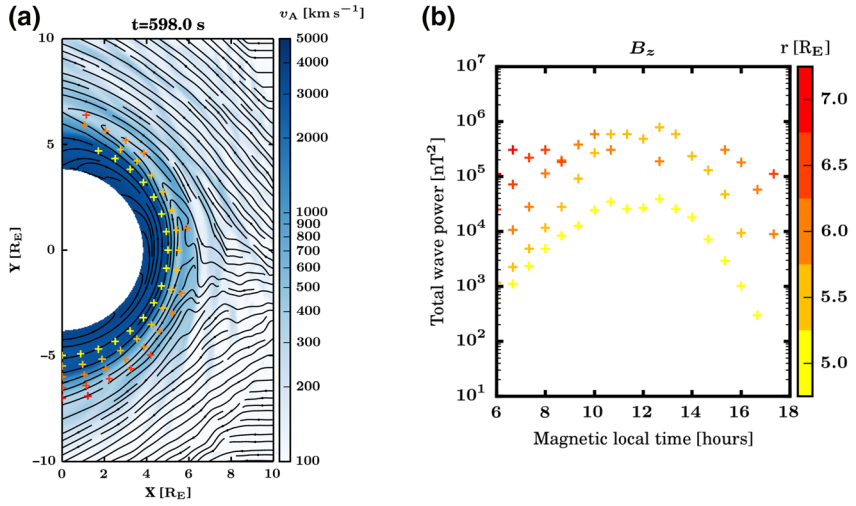

Figure 14. (a) Snapshot of the Alfvén velocity evaluated in the *X*-*Y* plane. The colored crosses are grid points at which wave power is evaluated. The black curves show plasma streamlines, with the flow deviation around the magnetosphere giving a good proxy of the magnetopause position. (b) Total wave power evaluated at the magnetospheric grid points shown in panel (a) and plotted as a function of magnetic local time.

we look for signatures of compressional waves in the outer magnetosphere, corresponding to the fast mode waves.

Figure 13a shows a snapshot of the perturbation of the B_z component in the *X*-*Y* plane. The perturbation is the difference of the instantaneous value at 500 s into the simulation from the 50 s average ‹B_z› centered on that time step. The foreshock waves appear as coherent B_z (transverse) oscillations upstream of the dawn sector of the bow shock. These waves then transmit into the magnetosheath and the magnetosphere. To understand the spatial variation of the simulated waves in more detail, we examined the simulation results sampled at four virtual spacecraft (VS1–VS4). The locations of the spacecraft are marked by colored dots in Figure 13a and displayed at the upper right corner of the figure. Figure 13b and 13c show the B_z time series and the corresponding power spectra. Figures 13d–13f show the coherence spectra for three virtual spacecraft pairs.

VS1 and VS2, located in the foreshock at $X = 12.5\ R_E$ with a *Y* separation of 2.5 R_E, both see large-amplitude (15 nT peak-to-peak) quasi monochromatic (period ~12 s) oscillations. This results in similar power spectra for these two locations. The power spectra occupy a broad band, rising above the 10^{-1} nT^2/Hz level at ~30 mHz and falling below it at ~300 mHz, with multiple minor peaks. This confirms that the compressional waves that enter the magnetosphere have a more complex spectrum during magnetic clouds. The power peaks at 50 mHz–90 mHz but remains high even at 100 mHz. However, the spectral similarity does not mean that the spacecraft detected the same wave. In fact, the time series plots indicate wave packet structures with significant time separation between VS1 and VS2, and the coherence spectrum (Figure 13d) shows low values in the band of elevated wave power.

VS3 and VS4, located in the magnetosphere, see much lower amplitudes. As can be seen from Figure 13a, VS3 is near the subsolar point, while VS4 is farther down on the quasi parallel flank, similar to THEMIS-A and GOES-13 in the real observation. At VS3, the amplitude is ~20% of those at VS1 and VS2. Note that in Figure 13b the amplitude at VS3 (VS4) is magnified by a factor of 5 (25). Although the spectrum at VS3 is elevated at >50 mHz as is the case in the foreshock at the VS1 and VS2 locations (Figure 13c), the waves at VS3 show low coherence with the foreshock waves (Figure 13e). Within the magnetosphere, the amplitude is position dependent. At VS4, the amplitude is ~20% of that at VS3, consistent with the amplitude ratio between THEMIS-A and GOES-13 that can be deduced from Figure 11f. In addition, the spectrum at VS4 does not exhibit a broad peak at >40 mHz, unlike at VS3. Not surprisingly, the VS3-VS4 coherence is low in the band (50–90 mHz) of strong foreshock waves (Figure 13f).

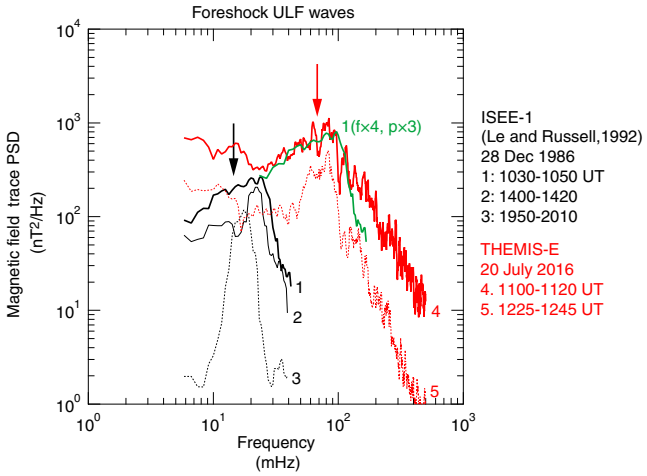

Figure 15. Comparison of magnetic field trace power in the ion foreshock for different IMF conditions. The spectra shown in black are generated from magnetic fields measured by ISEE-1 as it moved sunward during the time period studied by Le and Russell (1992). The spectra shown in red are generated from magnetic fields measured by THEMIS-E for time intervals when it was just outside the magnetosheath (spectrum 4, thick line) and just earthward of the foreshock boundary with the solar wind (spectrum 5, thin line). The spectrum shown in green is the same as ISEE-1 spectrum 1 but with the frequency shifted upward by a factor of 4 and the power raised by a factor of 3. IMF, interplanetary magnetic field.

The simulation results indicate that within the magnetosphere the wave amplitude changes with MLT and distance from the magnetopause (see also Figure 14b). The low amplitude at VS4 can be attributed to the large distance of the spacecraft from noon and from the magnetopause compared with VS3. Although the simulation does not cover the midnight sector, this position dependence can explain the difference in the wave amplitude observed at GOES-13, -14, and -15 presented in Figure 11. GOES-13 was located closest to midnight and farthest from the magnetopause and detected the lowest amplitude. GOES-15, located closest to noon and the magnetopause, detected the highest amplitude.

The spatial variation of ULF wave power in the Pc3 band is well documented. Spacecraft studies by Heilig et al. (2007) showed that the wave power decreases with solar zenith angle for all IMF orientations. Tanaka et al. (2004) found that Pc3 wave power on the ground is peaked at 1030–1130 local time, but with wave activity extending to both the morning and the afternoon sectors. Takahashi and Anderson (1992) found that in the equatorial magnetosphere the B_t power at a Pc3 frequency (26 mHz) peaks at L~5 in the 1000–1200 MLT sector and that the wave power decreases rapidly toward the midnight sector. These previous results are qualitatively consistent with the observational results shown in Figure 11.

These observations motivated us to examine the dependence of the intensity of the simulated magnetospheric waves on geocentric distance and local time. Figure 14a shows the magnetospheric grid points selected for evaluating the wave power. At all these virtual spacecraft locations, compressional waves are observed (defined as wave power in B_t > 10× wave power in B_x). Figure 14b shows the total wave power summed over the frequencies between 50 and 125 mHz (corresponding to the frequencies of the foreshock waves) for B_z. The plots are generated by extracting magnetic field time series data at each position for the last 250 s of the simulation and computing the wavelet power spectrum of each magnetic field component and the magnitude (B_t). The figure shows that compressional wave power appears both on the dawn and on the dusk sides of the magnetosphere, with the peak power very close to local noon. At the deepest locations within the magnetosphere (yellow crosses), the power at 08 h MLT is an order of magnitude higher than at 16 h MLT. This is also the case farther outward, indicating that the domain of strong foreshock waves maps more or less directly to the magnetosphere.

As noted earlier, the magnetosheath thickness is larger in our simulation than observed, most likely due to the 2-D simulation domain. This may reduce the wave power entering the magnetosphere, as the waves may be more strongly attenuated as they cross a wider magnetosheath. Our results may thus underestimate the wave power in the magnetosphere. Furthermore, the magnetosheath flow pattern is modified when the magnetosheath is broader. This effect is strongest on the flanks, while streamlines in the subsolar magnetosheath are the least affected (e.g. Soucek & Escoubet, 2012). Only the latter are relevant to the transmission of foreshock waves, because the magnetosheath flow pattern is such that only the streamlines originating from the subsolar bow shock will reach the magnetopause (Soucek & Escoubet, 2012; Spreiter et al., 1966). Therefore, we do not expect a larger magnetosheath thickness to affect noticeably the local time distribution of wave power in the magnetosphere.

8. Discussion

The objective of the present study is to characterize ULF waves during a period of a magnetic cloud with an enhanced magnetic field. We discuss our results concerning this objective by making reference to previous studies.

8.1. Waves in the Foreshock

As a demonstration of the importance of our observations, we show in Figure 15 a comparison of magnetic field trace spectra at THEMIS-E during our event and at International Sun-Earth Explorer 1 (ISEE-1) during a foreshock traversal event reported by Le and Russell (1992). A trace spectrum is the sum of the power spectra of three orthogonal field components. The time resolution of the data used for the spectra is 1 s for THEMIS-E and 4 s for ISEE-1. The ISEE-1 data are actually oversampled 12-s averages, so we show only frequencies below the Nyquist frequency, 42 mHz, of 12 s samples. The spectra are smoothed in the frequency domain by taking 7-point running averages. The three ISEE-1 spectra are for 20 min intervals taken just sunward of the bow shock (spectrum 1), at the mid part of the foreshock (spectrum 2), and just earthward of the foreshock-solar wind boundary (spectrum 3). These are part of three 65-min segments shown in Figure 8 of Le and Russell (1992). We use 20 min segments from ISEE-1 to be consistent with the THEMIS-E spectra, which uses measurements made at 1100 UT–1120 UT just sunward of the bow shock (spectrum 4, thick red line) and at 1225 UT–1245 UT just earthward of the foreshock boundary with the solar wind (spectrum 5, thin red line). The spectrum shown in green is spectrum 1 at ISEE-1 that is multiplied by 4 in frequency and 3 in intensity.

There are notable differences between the THEMIS-E and ISEE-1 spectra. First, the THEMIS-E spectra show wave power at frequencies much higher, by a factor of ∼4, than those at ISEE-1. The frequency difference is attributed to the difference in the IMF conditions. The average values of B_t and θ_{xB}, evaluated using the ISEE-1 data, are (3.9 nT, 48°), (3.7 nT, 36°), and (2.5 nT, 30°) for ISEE-1 spectra-1, -2, and -3. The corresponding f_{fw} values are 13 (black arrow), 17, and 15 mHz. For THEMIS-E spectra-4 and -5, we have (17.4 nT, 44°) and (13.4 nT, 27°) and the corresponding f_{fw} values of 68 mHz (red arrow) and 81 mHz. The f_{fw} ratio is 4.4 between THEMIS-E (spectrum 4) and ISEE-1 (spectrum 1), which is in good agreement with the observation. At both spacecraft, f_{fw} is located below the frequency of the spectral peak. This likely occurs because each observation was made in the foreshock region where the angle between the local shock normal and the IMF (denoted θ_{nB}) is smaller than θ_{xB} (De Lauretis et al., 2010).

The spectral intensity and shape also differ between THEMIS-E and ISEE-1. Comparing the spectra (1 and 4) just sunward of the bow shock, we find that the peak power at THEMIS-E is ∼3 times higher than that at ISEE-1. In addition, we find that the power at >100 mHz falls more rapidly in the frequency-shifted ISEE-1 spectrum. At larger distances from the bow shock (spectra-2, -3, and -5), the most dominant spectral peak becomes sharper and weaker, but the difference between ISEE-1 and THEMIS-A is basically the same in term of the peak frequency and the spectral shape.

The larger peak power in the THEMIS observations could be due to the high solar wind density during the interval under study, ∼12 cm^{-3}, much larger than what is typically observed at Earth (∼6 cm^{-3}). Given that both the Alfvén and magnetosonic Mach numbers having fairly typical values (∼7 and ∼5.5) during this event, the fraction of solar wind particles reflected off the shock front should be comparable to what is observed during regular solar wind conditions. However, because of the high solar wind density, the number density of backstreaming ions is expected to be higher than usual in such conditions. This would, in turn, result in higher foreshock wave amplitude, because the growth rate of the waves increases with increasing backstreaming density (Gary, 1993). Unfortunately, the lack of a solar wind monitor during the ISEE-1 foreshock observations prevents us from confirming this hypothesis for the events presented here. A more detailed comparison of the wave power in the foreshock during regular solar wind conditions and magnetic clouds is left for future work.

8.2. Waves in the Magnetosphere and Pulsations on the Ground

A number of studies reported a high degree of similarity between the frequencies of compressional magnetic field oscillations in the magnetosphere and ground magnetic pulsations at times of low IMF cone angle (Chi et al., 1994; Clausen et al., 2009; Francia et al., 2012; Le & Russell, 1992; Odera et al., 1991; Ponomarenko et al., 2010; Takahashi et al., 2016). This is not the case in the present study. To demonstrate this point, we generated Figure 16, which contrasts magnetic field power spectra under different solar wind conditions.

Figures 16a–16e show a reanalysis of the ULF wave event on 5 September 2002 reported by Clausen et al. (2009). We have chosen a 20 min interval (1830 UT–1850 UT) of low IMF cone angle and computed magnetic field power spectra of foreshock waves detected by Geotail (Kokubun et al., 1994), magnetospheric compressional waves detected by Cluster-3 (Balogh et al., 1997), and ground magnetic pulsations detected

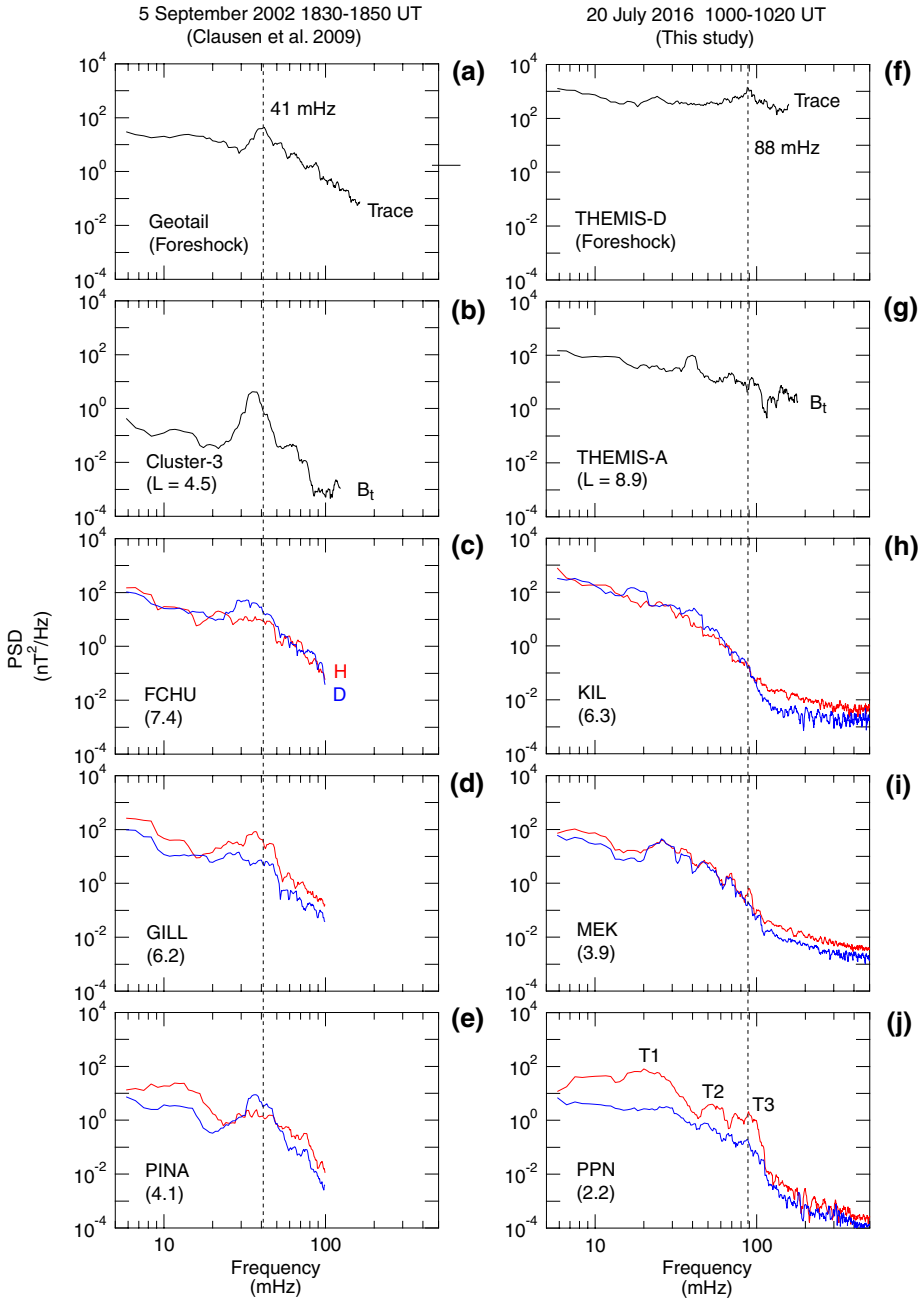

Figure 16. Comparison ULF wave spectra under different solar wind conditions. (a-e) Magnetic field spectra in the ion foreshock (Geotail), in the magnetosphere (Cluster-3), and on the ground (FCHU, GILL, and PINA) during a wave event reported by Clausen et al. (2009). *L* values are shown in parentheses for Cluster-3 and the ground stations. The vertical dashed line indicates the theoretical foreshock wave frequency f_{fw} for the magnetic field measured by Geotail. (f-j) Similarly arranged magnetic field spectra for a 20-min interval included in the present study. ULF, ultralow-frequency.

by the Canadian Array for Realtime Investigations of Magnetic Activity (CARISMA) magnetometers (Mann et al., 2008) located at Fort Churchill (FCHU), Gillam (GILL), and Pinawa (PINA). We show the trace spectrum at Geotail, the B_t spectrum at Cluster-3, and the *H* and *D* spectra on the ground. The black vertical dashed line at 41 mHz indicates the f_{fw} value corresponding to the magnetic field measured at Geotail. The spectra show peaks near f_{fw} both in space and on the ground. Clausen et al. (2009) took this as evidence for transmission of monochromatic foreshock waves into the magnetosphere.

Figures 16f–16j show the magnetic field spectra for a 20 min time period during our own wave event, with the sources being THEMIS-D (foreshock), THEMIS-A (magnetosphere), and the three EMMA stations KIL, MEK, and PPN. In this example, we get f_{fw} = 88 mHz using the magnetic field measured by THEMIS-D. The THEMIS-D spectrum is peaked at this frequency, consistent with the Geotail spectrum in the Clausen et al. (2009) event that shows a peak at the theoretical frequency (41 mHz) given for that event. However, no corresponding spectral enhancement is detected in the magnetosphere or on the ground except at PPN. At this station, a peak occurs near 88 mHz in the *H* spectrum. Because the peak corresponds to the T3 wave frequency (see Figure 10), the spectral peak could be the result of field line resonance excited by the 88 mHz foreshock waves, which appear to produce a minor peak in the *D* spectra at multiple latitudes. Alternatively, the T3 waves could be transient waves excited by broadband disturbances coming from the foreshock, as we discussed in Section 5.2. Another feature, which is found at all ground stations, is the change of the spectral shape at ~100 mHz. Across this frequency, the slope of the spectra in log-log display changes from steep to shallow. This could be caused by the reduction of the foreshock wave power above f_{fw}.

8.3. Local Time Variation of Wave Amplitude

During the magnetic cloud interval, ULF waves of foreshock origin did not produce any notable power enhancement on the nightside. This is different from some previous observations reporting otherwise (Takahashi et al., 2016). It is possible that the difference comes from the IMF orientation. The wave event studied by Takahashi et al. (2016) was observed when the IMF was aligned with the average Parker spiral (θ_{xB}~45°). This meant that a quasi-parallel shock was formed in the dawn terminator, sending foreshock wave power from there to the midnight sector of the inner magnetosphere. During the time interval selected in our study, the IMF cone angle was smaller, which means that a parallel shock was formed closer to noon. If the foreshock wave power enters the magnetosphere from that local time, the waves may be deflected by the plasmasphere and do not reach the midnight sector. This scenario could be tested by conducting a statistical analysis of the dependence of the global distribution of magnetospheric compressional ULF waves on IMF orientation.

Another, more plausible, explanation is that the magnetospheric compressional waves in the present study had short scale lengths in the azimuthal (MLT) direction. This is inferred from the simulation results shown in Figure 13. The simulated foreshock waves have short coherence scale lengths in the direction perpendicular to the background IMF, consistent with the finding for other magnetic cloud events (Turc et al., 2019). Upon interaction with the magnetosphere, these waves produce magnetospheric compressional waves also having short scale lengths in the direction tangential to the magnetopause. This means that the effective azimuthal wave number (m) of the magnetospheric waves is large. When m is large, fast mode waves behaves like surface waves (Lee, 1996; Wolfe & Kaufmann, 1975) meaning that the amplitude decreases quickly with distance from the magnetopause. In this case, the waves will be highly attenuated when they reach spacecraft located at large distances from the magnetopause (e.g., GOES-13, -14, and -15), making their detection by the spacecraft difficult.

9. Conclusions

We have studied the relationship among ULF waves in the ion foreshock, in the magnetosphere, and on the ground to understand how the waves propagate during the passage of a magnetic cloud, which is characterized by an IMF with high magnitudes and low cone angles. As we reviewed in Section 1, many observational studies examined foreshock ULF waves and their relation to magnetospheric ULF waves, but in most of these studies the IMF magnitude was lower than that (~14 nT) observed during our magnetic cloud event. Therefore, the event provided us with a unique opportunity to examine whether ULF waves in the foreshock and the magnetosphere are different when the IMF magnitude is unusually high. We studied the wave event by analyzing data from multiple spacecraft and ground magnetometers and by conducting a numerical simulation that is capable of describing not only foreshock ULF waves with high spatial and temporal resolutions but also how waves transmitted into the magnetosphere propagate, although the mag-

netospheric part of the simulation is limited by the fact that realistic background magnetospheric plasma cannot be produced because of the 2-D setup. We found that ULF waves in our study differ from those observed under normal IMF conditions as summarized below:

1. Waves observed in the foreshock show a spectral peak at ~90 mHz, much higher than the frequencies of foreshock waves observed at times of average IMF magnitudes. While this is expected from the well-established wave generation mechanism involving ion-cyclotron resonance, we also found that the spectral peak is broader and the spectral power is higher during the magnetic cloud interval. According to a previous study (Turc et al., 2019), the broader spectral peak may be explained by changes in the suprathermal ion properties during magnetic clouds. The large spectral power is likely due to the high solar wind density in this event, which results in a large suprathermal ion density in the foreshock, conducive to a larger wave growth rate
2. A spacecraft located in the dayside magnetosphere detected fast mode waves that can be attributed to transmitted foreshock waves. However, spacecraft located in the night-side magnetosphere did not detect compressional magnetic field oscillations at the foreshock wave frequency, unlike at times of average IMF magnitudes. The numerical simulation indicates that the MLT dependence of wave intensity maps from the foreshock to the magnetosphere, which explains the spacecraft observation. In addition, the simulation indicates that foreshock waves have short spatial scale lengths compared to those excited under average IMF conditions. Such waves cannot penetrate deep into the magnetosphere, also explaining the night-side spacecraft observation made away from the magnetopause
3. Ground magnetometers located near noon at $L = 1.6–6.5$ did not detect outstanding oscillations at a latitude-independent frequency matching the foreshock wave frequency, unlike at times of average IMF magnitudes. However, a reduction or cutoff of D-component power was observed at $L < 5$ above ~100 mHz, which could be related to the foreshock wave power peaked at ~90 mHz. We also note that even if 90-mHz foreshock waves propagate into the magnetosphere, they cannot couple to the fundamental toroidal (T1) waves at $L = 1.6–6.5$ by the field line resonance mechanism, because the T1 frequencies are lower than 90 mHz in that region. At times of average IMF magnitudes, the frequency of foreshock waves is lower than 90 mHz and the waves can excite T1 waves at midlatitude stations. The absence of T1 field line resonance driven by foreshock waves is a feature unique to times of high IMF magnitudes

Data Availability Statement

Data used in this study are available from the following sources: NOAA National Geophysical Data Center (http://satdat.ngdc.noaa.gov) for GOES; Japan Aerospace Exploration Agency, Japan (https://darts.isas.jaxa.jp/stp/geotail) for Geotail; NASA Goddard Space Flight Center (https://omniweb.gsfc.nasa.gov/ow.html), for OMNI; NASA/GSFC Space Physics Data Facility Coordinated Data Analysis Web (https://cdaweb.gsfc.nasa.gov/index.html) for Cluster; Zenodo **(**http://doi.org/10.5281/zenodo.4047199**)**, for EMMA; University of Alberta CARISMA Data Repository (https://www.carisma.ca/carisma-data-repository) for CARISMA; and World Data Center for Geomagnetism, Kyoto (http://wdc.kugi.kyoto-u.ac.jp), for geomagnetic indices. The Vlasiator run described here takes several terabytes of disk space and is kept in storage maintained within the CSC-IT Center for Science. It can be accessed through the following link: https://a3s.fi/swift/v1/AUTH_81f1cd490d494224880ea77e4f98490d/vlasiator-2d-afc. Usage of Vlasiator data must comply with the data policy as described on the Vlasiator website (https://www.helsinki.fi/en/researchgroups/vlasiator/rules-of-the-road). Vlasiator uses a data structure developed in house (https://github.com/fmihpc/vlsv/, Sandroos, 2019), which can be read using the Analysator software (https://github.com/fmihpc/analysator/, Battarbee & the Vlasiator team, 2020).

References

Allan, W., Menk, F. W., Fraser, B. J., Li, Y., & White, S. P. (1996). Are low-latitude Pi2 pulsations cavity/waveguide modes? *Geophysical Research Letters*, *23*(7), 765–768. https://doi.org/10.1029/96gl00661

Acknowledgments
The authors thank I. R. Mann, D. K. Milling, and the rest of the CARISMA team for data. CARISMA is operated by the University of Alberta, funded by the Canadian Space Agency. The authors also thank the Cluster FGM team and ESA Cluster Science Archive for the Cluster data. K. Takahashi is grateful to Guan Le for her comments on the ISEE magnetometer data. This study was initiated during the workshop entitled "Global study of the transmission of foreshock ULF waves into the magnetosheath and the magnetosphere" hosted by International Space Science Institute, Bern. Work at the Johns Hopkins University Applies Physics Laboratory was supported by NASA Grant NNX-17AD34G and NSF Grant OPP-1744609. The work of L. T. is supported by the Academy of Finland (grant number 322544). The authors acknowledge the European Research Council for Starting grant 200141-QuESpace, with which Vlasiator (http://helsinki.fi/vlasiator) was developed, and Consolidator grant 682068-PRESTISSIMO awarded to further develop Vlasiator and use it for scientific investigations. We gratefully also acknowledge the Academy of Finland Grants 309937 and 312351, which support Vlasiator development and science as well. The run shown in this paper was carried out on the Sisu supercomputer at the CSC–IT Center for Science in Finland, thanks to a Grand Challenge award. The work of N. T. was supported by Japan Society for the Promotion of Science Grants 16H06286 and 18KK0099.

Auster, H. U., Glassmeier, K. H., Magnes, W., Aydogar, O., Baumjohann, W., Constantinescu, D., & Wiedemann, M. (2008). The THEMIS fluxgate magnetometer. *Space Science Reviews*, *141*(1–4), 235–264. https://doi.org/10.1007/s11214-008-9365-9

Balogh, A., Dunlop, M. W., Cowley, S. W. H., Southwood, D. J., Thomlinson, J. G., Glassmeier, K. H., & Kivelson, M. G. (1997). The Cluster magnetic field investigation. *Space Science Reviews*, *79*(1/2), 65–91. https://doi.org/10.1023/a:1004970907748

Barnes, A. (1970). Theory of generation of bow-shock-associated hydromagnetic waves in the upstream interplanetary medium. *Cosmic Electrodynamics*, *1*, 90–114.

Battarbee, M., & the Vlasiator Team. (2020). *Analysator: python analysis toolkit*. Github repository. https://github.com/fmihpc/analysator/

Bilitza, D., Altadill, D., Truhlik, V., Shubin, V., Galkin, I., Reinisch, B., & Huang, X. (2017). International Reference Ionosphere 2016: From ionospheric climate to real-time weather predictions. *Space Weather*, *15*(2), 418–429. https://doi.org/10.1002/2016sw001593

Bonnell, J. W., Mozer, F. S., Delory, G. T., Hull, A. J., Ergun, R. E., Cully, C. M., & Harvey, P. R. (2008). The Electric Field Instrument (EFI) for THEMIS. *Space Science Reviews*, *141*(1–4), 303–341. https://doi.org/10.1007/s11214-008-9469-2

Burlaga, L. F., Sittler, E., Mariani, F., & Schwenn, R. (1981). Magnetic loop behind an interplanetary shock - Voyager, Helios, and IMP 8 observations. *Journal of Geophysical Research*, *86*, 6673–6684. https://doi.org/10.1029/JA086iA08p06673

Chi, P. J., Russell, C. T., & Le, G. (1994). Pc-3 and Pc-4 activity during a long-period of low interplanetary magnetic-field cone angle as detected across the Institute of Geological Sciences array. *Journal of Geophysical Research*, *99*(A6), 11127–11139. https://doi.org/10.1029/94ja00517

Clausen, L. B. N., & Glassmeier, K. H. (2014). Enhancement of ultralow frequency wave amplitudes at the plasmapause. *Journal of Geophysical Research: Space Physics*, *119*(11), 9113–9124. https://doi.org/10.1002/2014ja020072

Clausen, L. B. N., Yeoman, T. K., Fear, R. C., Behlke, R., Lucek, E. A., & Engebretson, M. J. (2009). First simultaneous measurements of waves generated at the bow shock in the solar wind, the magnetosphere and on the ground. *Annales Geophysicae*, *27*(1), 357–371. https://doi.org/10.5194/angeo-27-357-2009

De Lauretis, M., Francia, P., Regi, M., Villante, U., & Piancatelli, A. (2010). Pc3 pulsations in the polar cap and at low latitude. *Journal of Geophysical Research*, *115*(A11), A11223. https://doi.org/10.1029/2010ja015967

Del Corpo, A., Vellante, M., Heilig, B., Pietropaolo, E., Reda, J., & Lichtenberger, J. (2019). Observing the cold plasma in the Earth's magnetosphere with the EMMA network. *Annals of Geophysics*, *62*(4), GM447. https://doi.org/10.4401/ag-7751

Eastwood, J. P., Balogh, A., Lucek, E. A., Mazelle, C., & Dandouras, I. (2005). Quasi-monochromatic ULF foreshock waves as observed by the four-spacecraft Cluster mission: 1. Statistical properties. *Journal of Geophysical Research*, *110*(A11), A11219. https://doi.org/10.1029/2004JA010617

Engebretson, M. J., Zanetti, L. J., Potemra, T. A., Baumjohann, W., Lühr, H., & Acuna, M. H. (1987). Simultaneous observation of Pc 3–4 pulsations in the solar wind and in the Earth's magnetosphere. *Journal of Geophysical Research*, *92*(A9), 10053–10062. https://doi.org/10.1029/JA092iA09p10053

Fairfield, D. H. (1969). Bow shock associated waves observed in the far upstream interplanetary medium. *Journal of Geophysical Research*, *74*(14), 3541–3553. https://doi.org/10.1029/JA074i014p03541

Fairfield, D. H. (1971). Average and unusual locations of the Earth's magnetopause and bow shock. *Journal of Geophysical Research*, *76*(28), 6700–6716. https://doi.org/10.1029/JA076i028p06700

Farris, M. H., & Russell, C. T. (1994). Determining the standoff distance of the bow shock: Mach number dependence and use of models. *Journal of Geophysical Research*, *99*(A9), 17681–17689. https://doi.org/10.1029/94ja01020

Francia, P., Regi, M., De Lauretis, M., Villante, U., & Pilipenko, V. A. (2012). A case study of upstream wave transmission to the ground at polar and low latitudes. *Journal of Geophysical Research*, *117*(A1). https://doi.org/10.1029/2011ja016751

Gary, S. P. (1993). *Theory of space plasma microinstabilities*, (pp. 1–179). New York, NY: Cambridge University Press.

Greenstadt, E. W., & Olson, J. V. (1976). Pc 3, 4 activity and interplanetary field orientation. *Journal of Geophysical Research*, *81*(34), 5911–5920. https://doi.org/10.1029/JA081i034p05911

Hartinger, M., Moldwin, M. B., Angelopoulos, V., Takahashi, K., Singer, H. J., Anderson, R. R., & Wygant, J. R. (2010). Pc5 wave power in the quiet-time plasmasphere and trough: CRRES observations. *Geophysical Research Letters*, *37*, L07107. https://doi.org/10.1029/2010GL042475

Heilig, B., Lühr, H., & Rother, M. (2007). Comprehensive study of ULF upstream waves observed in the topside ionosphere by CHAMP and on the ground. *Annales Geophysicae*, *25*(3), 737–754. https://doi.org/10.5194/angeo-25-737-2007

Hoppe, M. M., Russell, C. T., Frank, L. A., Eastman, T. E., & Greenstadt, E. W. (1981). Upstream hydromagnetic waves and their association with backstreaming ion populations: ISEE 1 and 2 observations. *Journal of Geophysical Research*, *86*(A6), 4471–4492. https://doi.org/10.1029/JA086iA06p04471

Hughes, W. J., & Southwood, D. J. (1976). The screening of micropulsation signals by the atmosphere and ionosphere. *Journal of Geophysical Research*, *81*(19), 3234–3240. https://doi.org/10.1029/JA081i019p03234

King, J. H., & Papitashvili, N. E. (2005). Solar wind spatial scales in and comparisons of hourly Wind and ACE plasma and magnetic field data. *Journal of Geophysical Research*, *110*, A02104. https://doi.org/10.1029/2004JA010649

Kokubun, S., Yamamoto, T., Acuna, M. H., Hayashi, K., Shiokawa, K., & Kawano, H. (1994). The Geotail magnetic field experiment. *Journal of Geomagnetism and Geoelectricity*, *46*(1), 7–21. https://doi.org/10.5636/jgg.46.7

Kovner, M. S., Lebedev, V. V., Plyasova-Bakounina, T. A., & Troitskaya, V. A. (1976). On the generation of low-frequency waves in the solar wind in the front of the bow shock. *Planetary and Space Science*, *24*(3), 261–267. https://doi.org/10.1016/0032-0633(76)90022-2

Lee, D. H. (1996). Dynamics of MHD wave propagation in the low-latitude magnetosphere. *Journal of Geophysical Research*, *101*(A7), 15371–15386. https://doi.org/10.1029/96ja00608

Le, G., & Russell, C. T. (1992). A study of ULF wave foreshock morphology-II: Spatial variation of ULF waves. *Planetary and Space Science*, *40*(9), 1215–1225. https://doi.org/10.1016/0032-0633(92)90078-3

Lichtenberger, J., Clilverd, M. A., Heilig, B., Vellante, M., Manninen, J., Rodger, C. J., & Simon-Wedlund, M. (2013). The plasmasphere during a space weather event: First results from the PLASMON project. *Journal of Space Weather and Space Climate*, *3*, A23. https://doi.org/10.1051/swsc/2013045

Mann, I. R., Milling, D. K., Rae, I. J., Ozeke, L. G., Kale, A., Kale, Z. C., & Singer, H. J. (2008). The upgraded CARISMA magnetometer array in the THEMIS era. *Space Science Reviews*, *141*(1–4), 413–451. https://doi.org/10.1007/s11214-008-9457-6

McFadden, J. P., Carlson, C. W., Larson, D., Bonnell, J., Mozer, F., Angelopoulos, V., & Auster, U. (2008). THEMIS ESA first science results and performance issues. *Space Science Reviews*, *141*(1–4), 477–508. https://doi.org/10.1007/s11214-008-9433-1

McKenzie, J. F. (1970). Hydromagnetic wave interaction with the magnetopause and the bow shock. *Planetary and Space Science*, *18*(1), 1–23. https://doi.org/10.1016/0032-0633(70)90063-2

Mozer, F. S. (1973). Analyses of techniques for measuring DC and AC electric fields in the magnetosphere. *Space Science Reviews*, *14*(2), 272–313. https://doi.org/10.1007/bf02432099

Odera, T. J., Van Swol, D., Russell, C. T., & Green, C. A. (1991). Pc 3,4 magnetic pulsations observed simultaneously in the magnetosphere and at multiple ground stations. *Geophysical Research Letters*, *18*(9), 1671–1674. https://doi.org/10.1029/91gl01297

Palmroth, M., Archer, M., Vainio, R., Hietala, H., Pfau-Kempf, Y., Hoilijoki, S., & Eastwood, J. P. (2015). ULF foreshock under radial IMF: THEMIS observations and global kinetic simulation Vlasiator results compared. *Journal of Geophysical Research: Space Physics*, *120*(10), 8782–8798. https://doi.org/10.1002/2015JA021526

Palmroth, M., Ganse, U., Pfau-Kempf, Y., Battarbee, M., Turc, L., Brito, T., & von Alfthan, S. (2018). Vlasov methods in space physics and astrophysics. *Living Reviews in Computational Astrophysics*, *4*, 1. https://doi.org/10.1007/s41115-018-0003-2

Palmroth, M., Pulkkinen, T. I., Janhunen, P., & Wu, C. C. (2003, January). Stormtime energy transfer in global MHD simulation. *Journal of Geophysical Research*, *108*(A1), 1048. https://doi.org/10.1029/2002JA009446

Petrinec, S. M., Yumoto, K., Lühr, H., Orr, D., Milling, D., Hayashi, K., & Araki, T. (1996). The CME event of February 21, 1994: Response of the magnetic field at the Earth's surface. *Journal of Geomagnetism and Geoelectricity*, *48*(11), 1341–1379. https://doi.org/10.5636/jgg.48.1341

Pfau-Kempf, Y., Battarbee, M., Ganse, U., Hoilijoki, S., Turc, L., von Alfthan, S., & Palmroth, M. (2018). On the importance of spatial and velocity resolution in the hybrid-Vlasov modeling of collisionless shocks. *Frontiers in Physics*, *6*(44). https://doi.org/10.3389/fphy.2018.00044

Ponomarenko, P. V., Walters, C. L., & St-Maurice, J. P. (2010). Upstream Pc3–4 waves: Experimental evidence of propagation to the nightside plasmapause/plasmatrough. *Geophysical Research Letters*, *37*, L22102. https://doi.org/10.1029/2010gl045416

Poulter, E. M., & Nielsen, E. (1982). The hydromagnetic oscillation of individual shells of the geomagnetic-field. *Journal of Geophysical Research*, *87*(A12), 432–438. https://doi.org/10.1029/JA087iA12p10432

Roux, A., LeÂ Contel, O., Coillot, C., Bouabdellah, A., deÂ la Porte, B., Alison, D., & Vassal, M. C. (2008). The search coil magnetometer for THEMIS. *Space Science Reviews*, *141*(1–4), 265–275. https://doi.org/10.1007/s11214-008-9455-8

Russell, C. T., Luhmann, J. G., Odera, T. J., & Stuart, W. F. (1983). The rate of occurrence of dayside Pc 3,4 pulsations: The *L*-value dependence of the IMF cone angle effect. *Geophysical Research Letters*, *10*(8), 663–666. https://doi.org/10.1029/GL010i008p00663

Sandroos, A. (2019). *Vlsv: File format and tools*. Github repository. https://github.com/fmihpc/vlsv/

Shue, J. H., Song, P., Russell, C. T., Steinberg, J. T., Chao, J. K., Zastenker, G., & Kawano, H. (1998). Magnetopause location under extreme solar wind conditions. *Journal of Geophysical Research*, *103*(A8), 17691–17700. https://doi.org/10.1029/98ja01103

Singer, H. J., Matheson, L., Grubb, R., Newman, A., & Bouwer, S. D. (1996). Monitoring space weather with the GOES magnetometers. Proceedings of the society of photo-optical instrumentation engineers (SPIE), 2812, 299–308. https://doi.org/10.1117/12.254077

Singer, H. J., Southwood, D. J., Walker, R. J., & Kivelson, M. G. (1981). Alfven wave resonances in a realistic magnetospheric magnetic field geometry. *Journal of Geophysical Research*, *86*(A6), 4589–4596. https://doi.org/10.1029/JA086iA06p04589

Soucek, J., & Escoubet, C. P. (2012). Predictive model of magnetosheath plasma flow and its validation against Cluster and THEMIS data. *Annales Geophysicae*, *30*, 973–982. https://doi.org/10.5194/angeo-30-973-2012

Spreiter, J. R., Summers, A. L., & Alksne, A. Y. (1966). Hydromagnetic flow around the magnetosphere. *Planetary and Space Science*, *14*, 223. https://doi.org/10.1016/0032-0633(66)90124-3

Sugiura, M., & Wilson, C. R. (1964). Oscillation of the geomagnetic field lines and associated magnetic perturbations at conjugate points. *Journal of Geophysical Research*, *69*(7), 1211–1216. https://doi.org/10.1029/JZ069i007p01211

Takahashi, K., & Anderson, B. J. (1992). Distribution of ULF energy ($f < 80$ mHz) in the inner magnetosphere: A statistical analysis of AMPTE CCE magnetic field data. *Journal of Geophysical Research*, *97*(A7), 10751. https://doi.org/10.1029/92ja00328

Takahashi, K., Anderson, B. J., Newell, P. T., Yamamoto, T., & Sato, N. (1994a). Propagation of compressional Pc 3 pulsations from space to the ground: A case study using multipoint measurements. In M. J. Engebretson, K. Takahashi, & M. Sholer (Eds.), Solar wind sources of magnetospheric ultra-low-frequency waves, geophysical monograph series (Vol. 81, pp. 355–363). Washington, DC: American Geophysical Union. https://doi.org/10.1029/GM081p0355

Takahashi, K., Bonnell, J., Glassmeier, K. H., Angelopoulos, V., Singer, H. J., Chi, P. J., & Liu, W. (2010). Multipoint observation of fast mode waves trapped in the dayside plasmasphere. *Journal of Geophysical Research*, *115*, A12247. https://doi.org/10.1029/2010JA015956

Takahashi, K., Hartinger, M. D., Malaspina, D. M., Smith, C. W., Koga, K., Singer, H. J., & Yoshikawa, A. (2016). Propagation of ULF waves from the upstream region to the midnight sector of the inner magnetosphere. *Journal of Geophysical Research: Space Physics*, *121*(9), 8428–8447. https://doi.org/10.1002/2016ja022958

Takahashi, K., & Heilig, B. (2019). *L* versus time structures of dayside magnetic pulsations detected by the European Quasi-Meridional Magnetometer Array. *Journal of Geophysical Research: Space Physics*, *124*(8), 6566–6584, https://doi.org/10.1029/2019ja026796

Takahashi, K., Kokubun, S., Matsuoka, H., Shiokawa, K., Yumoto, K., Nakamura, M., & Matsumoto, H. (1994b). Geotail observation of magnetosonic Pc 3 waves in the dayside magnetosphere. *Geophysical Research Letters*, *21*(25), 2899–2902. https://doi.org/10.1029/94gl01419

Takahashi, K., McPherron, R. L., & Terasawa, T. (1984). Dependence of the spectrum of Pc 3–4 pulsations on the interplanetary magnetic field. *Journal of Geophysical Research*, *89*(A5), 2770. https://doi.org/10.1029/JA089iA05p02770

Tamao, T. (1964). The structure of three-dimensional hydromagnetic waves in a uniform cold plasma. *Journal of Geomagnetism and Geoelectricity*, *16*(2), 89–114. https://doi.org/10.5636/jgg.16.89

Tanaka, Y. M., Yumoto, K., Yoshikawa, A., Shinohara, M., Kawano, H., & Kitamura, T. I. (2004). Longitudinal structure of Pc3 pulsations on the ground near the magnetic equator. *Journal of Geophysical Research*, *109*(A3), A03201. https://doi.org/10.1029/2003ja009903

Troitskaya, V. A., Plyasova-Bakounina, T. A., & Gul'Elmi, A. V. (1971). The connection of Pc2–4 pulsations with the interplanetary magnetic field. *Doklady Akademiia Nauk SSSR*, *197*, 1312–1314.

Tsyganenko, N. A. (1989). A magnetospheric magnetic field model with a warped tail current sheet. *Planetary and Space Science*, *37*(1), 5–20. https://doi.org/10.1016/0032-0633(89)90066-4

Turc, L., Ganse, U., Pfau-Kempf, Y., Hoilijoki, S., Battarbee, M., Juusola, L., & Palmroth, M. (2018). Foreshock properties at typical and enhanced interplanetary magnetic field strengths: Results from hybrid-Vlasov simulations. *Journal of Geophysical Research: Space Physics*, *123*(0), 5476–5493. https://doi.org/10.1029/2018JA025466

Turc, L., Roberts, O. W., Archer, M. O., Palmroth, M., Battarbee, M., Brito, T., & Dandouras, I. (2019). First observations of the disruption of the earth's foreshock wave field during magnetic clouds. *Geophysical Research Letters*, *46*(22), 12644–12653. https://doi.org/10.1029/2019gl084437

Verō, J., Lühr, H., Vellante, M., Best, I., Střeštik, J., Miletits, J. C., & Zieger, B. (1998). Upstream waves and field line resonances: Simultaneous presence and alternation in Pc3 pulsation events. *Annales Geophysicae*, *16*(1), 34–48. https://doi.org/10.1007/s00585-997-0034-1

von Alfthan, S., Pokhotelov, D., Kempf, Y., Hoilijoki, S., Honkonen, I., Sandroos, A., & Palmroth, M. (2014). Vlasiator: First global hybrid-Vlasov simulations of Earth's foreshock and magnetosheath. *Journal of Atmospheric and Solar-Terrestrial Physics*, *120*, 24–35. https://doi.org/10.1016/j.jastp.2014.08.012

Waters, C. L., Menk, F. W., & Fraser, B. J. (1991). The resonance structure of low latitude Pc3 geomagnetic pulsations. *Geophysical Research Letters*, *18*(12), 2293–2296. https://doi.org/10.1029/91gl02550

Wolfe, A., & Kaufmann, R. L. (1975). MHD wave transmission and production near the magnetopause. *Journal of Geophysical Research*, *80*(13), 1764–1775. https://doi.org/10.1029/JA080i013p01764

Wolfe, A., Lanzerotti, L. J., & Maclennan, C. G. (1980). Dependence of hydromagnetic energy spectra on solar wind velocity and interplanetary magnetic field direction. *Journal of Geophysical Research*, *85*(A1), 114–118. https://doi.org/10.1029/JA085iA01p00114

Yumoto, K., & Saito, T. (1983). Relation of compressional HM waves at GOES 2 to low-latitude Pc 3 magnetic pulsations. *Journal of Geophysical Research*, *88*(A12), 10041. https://doi.org/10.1029/JA088iA12p10041

Yumoto, K., Saito, T., Akasofu, S.-I., Tsurutani, B. T., & Smith, E. J. (1985). Propagation mechanism of daytime Pc 3–4 pulsations observed at synchronous orbit and multiple ground-based stations. *Journal of Geophysical Research*, *90*(A7), 6439. https://doi.org/10.1029/JA090iA07p06439

Yumoto, K., Saito, T., Tsurutani, B., Smith, E., & Akasofu, S.-I. (1984). Relationship between the IMF magnitude and Pc 3 magnetic pulsations in the magnetosphere. *Journal of Geophysical Research*, *89*(A11), 9731–9740. https://doi.org/10.1029/JA089iA11p0973